

METHANE, CARBON MONOXIDE, AND AMMONIA IN BROWN DWARFS AND SELF-LUMINOUS GIANT PLANETS

KEVIN J. ZAHNLE

NASA Ames Research Center, MS-245-3, Moffett Field, CA 94035; Kevin.J.Zahnle@NASA.gov

MARK S. MARLEY

NASA Ames Research Center, MS-245-3, Moffett Field, CA 94035; Mark.S.Marley@NASA.gov

Draft version September 3, 2018

ABSTRACT

We address disequilibrium abundances of some simple molecules in the atmospheres of solar composition brown dwarfs and self-luminous extrasolar giant planets using a kinetics-based 1D atmospheric chemistry model. Our approach is to use the full kinetics model to survey the parameter space with effective temperatures between 500 K and 1100 K. In all of these worlds equilibrium chemistry favors CH₄ over CO in the parts of the atmosphere that can be seen from Earth, but in most disequilibrium worlds favors CO. The small surface gravity of a planet strongly discriminates against CH₄ when compared to an otherwise comparable brown dwarf. If vertical mixing is like Jupiter's, the transition from methane to CO occurs at 500 K in a planet. Sluggish vertical mixing can raise this to 600 K; but clouds or more vigorous vertical mixing could lower this to 400 K. The comparable thresholds in brown dwarfs are 1100 ± 100 K. Ammonia is also sensitive to gravity, but unlike CH₄/CO, the NH₃/N₂ ratio is insensitive to mixing, which makes NH₃ a potential proxy for gravity. HCN may become interesting in high gravity brown dwarfs with very strong vertical mixing. Detailed analysis of the CO-CH₄ reaction network reveals that the bottleneck to CO hydrogenation goes through methanol, in partial agreement with previous work. Simple, easy to use quenching relations are derived by fitting to the complete chemistry of the full ensemble of models. These relations are valid for determining CO, CH₄, NH₃, HCN, and CO₂ abundances in the range of self-luminous worlds we have studied but may not apply if atmospheres are strongly heated at high altitudes by processes not considered here (e.g., wave breaking).

1. INTRODUCTION

Disequilibrium chemistry has been known in Jupiter's atmosphere for several decades (Prinn and Barshay 1977; Bézard et al. 2002) and has been expected and suspected in brown dwarf atmospheres from the time of their discovery (Fegley and Lodders 1996; Noll et al. 1997; Saumon et al. 2000). The most famous disequilibrium is an overabundance of CO relative to CH₄. This occurs in Jupiter and brown dwarfs when CO is dredged up from deep, hot layers of the atmosphere more quickly than chemical reactions with ambient hydrogen can convert it to CH₄. It is to be expected that similar processes take place in young, self-luminous extrasolar giant planets. But the apparent paucity of methane in the atmospheres of planets with effective temperatures comparable to those of methane-rich T-type brown dwarfs was underpredicted and has been met with surprise.

Among field brown dwarfs methane appears—by definition—at the L to T-type transition where their near-infrared colors turn to the blue at effective temperatures near 1200 K (Kirkpatrick 2005). The first directly imaged planets, however, were found to have effective temperatures below 1200 K and yet their near-infrared spectra were devoid of signs of methane in K band (e.g., Barman et al. 2011a). The best example is HR8799c: despite an effective temperature near 1100 K, in both low and high resolution spectra—particularly the high resolution spectrum taken by Konopacky et al. (2013)—methane has gone missing.

Surface gravity is the defining difference between extrasolar giant planets and brown dwarfs, and to date is the only proven difference, although there are great hopes for metallicity. Field brown dwarfs (hereafter BDs) have high surface gravities (g of order 10⁵ cm/s²) and therefore very compressed scale heights. Extrasolar giant planets (EGPs) have modest surface gravities (g of order 10³ cm/s²) and extended scale heights (e.g., Burrows et al. 1997; Saumon & Marley 2008)¹. A BD and a self-luminous EGP of the same composition and the same effective temperature will have similar optical depths as a function of temperature, at least in the absence of clouds; i.e., the function $T(\tau)$ is roughly the same. However, because $p \propto \tau g$, the BD has a much higher pressure at a given optical depth than does the EGP, and a BD is much cooler than the EGP at a given pressure. Because lower temperatures and higher pressure favor CH₄ in its struggle with CO, it has been pointed out that CH₄ will be more easily seen and CO less easily seen at lower gravity in BDs (Hubeny and Burrows 2007). Hence Barman et al. (2011a) suggested that the even lower gravity of HR8799b might be why no methane is seen in it. We agree. We will verify that the dependence on g is strong and leads to qualitatively different outcomes for BDs and self-luminous EGPs, a result implicit in previous work but far from fully appreciated.

¹ We do not intend to wade into the nomenclature battles here. For our purposes companion objects below $\sim 13 M_J$ are planets.

Previous studies of carbon speciation in BDs and EGPs have mostly focused on a few particular objects (Saumon et al. 2006; Geballe et al. 2009; Barman et al. 2011a,b; Moses et al. 2011; Line et al. 2011), or on hot highly irradiated EGPs (Moses et al. 2011; Visscher 2012), or used one of several quench approximations culled from the literature (Fegley and Lodders 1996; Saumon et al. 2000; Lodders and Fegley 2002; Hubeny and Burrows 2007), or various combinations of the above (Cooper and Showman 2006; Visscher and Moses 2011; Moses et al. 2013a,b). The basic idea is that CH_4 and CO will often be seen in disequilibrium because the chemical reactions that would enforce equilibrium don't have time enough to take place while the gas is cool (Prinn and Barshay 1977). The disequilibrium composition that results is described as “frozen-in” or “quenched.”

Quenching has been widely used to quantify discussions of CO-CH_4 and $\text{N}_2\text{-NH}_3$ disequilibria in a wide range of astrophysical problems, dating at least back to Prinn and Barshay (1977)'s study of CO in Jupiter. Earlier discussions of quenching can be found with respect to the $\text{N}_2\text{-O}_2\text{-NO}$ system that is important in thunderbolts (Chameides et al. 1979), meteor entry and rocket reentry (Park and Menees 1978), and explosions in Earth's atmosphere (Zel'dovich and Raizer 1967). In the quench approximation, the disequilibrium composition that one can observe is approximated by the equilibrium composition when the relevant chemical reaction time scale t_{chem} equals the relevant cooling timescale, which if due to mixing can be written t_{mix} (Prinn and Barshay 1977). There are many different prescriptions for defining t_{chem} and t_{mix} that we will discuss below. The history of quench schemes for jovian planets, exoplanets, and brown dwarfs has been comprehensively recounted in a series of recent papers by Moses and colleagues (Moses et al. 2010, 2011; Visscher and Moses 2011).

Here we do something different. We use a 1D chemical kinetics code coupled to p - T profiles from a detailed 1D atmospheric structure code to compute a galaxy of chemical compositions in a wide range of possible brown dwarfs and cooling EGPs. The code explicitly includes reverses of all reactions so that, in the absence of atmospheric physics, the chemical composition would relax to equilibrium at every height. Our strategy is to find the apparent quench points in all the models and analyze these for their systematic properties. We then fine tune our results by using them in quench approximations. Our objective is to describe the emergent properties of the chemical network as a whole. Our strategy differs from previous work that seeks to determine the one key rate-limiting step in a network of reactions, which is then treated as the effective reaction rate for the network as a whole.

We limit the study to self-luminous cooling worlds for which insolation is not (yet) thermally important. This includes brown dwarfs, free-floating planets, and young directly-imaged planets. This category includes most of the exoplanets for which good data can be obtained in the present or in the near future. What this limitation means for carbon speciation is that we are concerned only with the conversion of CO to CH_4 . Unlike Line et al. (2011), Visscher and Moses (2011), and Visscher (2012), we do not address the kinetic inhibition against oxidizing

CH_4 to CO . The latter is an issue in strongly irradiated planets that are warm at high altitudes where, if vertical mixing is fast and the temperature not too hot, CH_4 and its photochemical products will be overabundant (Line et al. 2010; Miller-Ricci Kempton et al. 2011; Morley et al. 2013). Methane oxidation could be an issue for BDs and cooling EGPs if the higher parts of their atmospheres are strongly heated by wave-breaking processes not taken into account in our radiative-convective model, but we do not further address this possibility here.

Quenching in the nitrogen system has also been the subject of many studies over the years (Abelson 1966; Chameides and Walker 1981; Prinn and Fegley 1987; Fegley and Lodders 1994, 1996; Saumon et al. 2006; Moses et al. 2010, 2011; Line et al. 2011). As with methane, the underabundance of ammonia in brown dwarfs cold enough to favor it has been attributed to disequilibrium chemistry (Saumon et al. 2006). The visibility of ammonia has been made the distinguishing characteristic of the Y dwarf, the newest, coldest, and possibly last member of the stellar spectral sequence (Cushing et al. 2011). The $\text{NH}_3\text{-N}_2\text{-HCN}$ system differs from CO and CH_4 in interesting ways that lead to significantly different behavior.

Finally, for completeness, we address quenching of CO_2 , a gas that can be relatively easy to observe from a space-based observatory and, because its abundance is sensitive to metallicity, can be relatively telling. CO_2 is not always thought of as a species subject to quenching (but see Prinn and Fegley (1987)). In the H_2 -rich, UV-poor worlds that are the subject of this study, CO_2 quenching does take place.

2. OVERVIEW OF CO AND CH_4

Figure 1 illustrates the most important chemical pathways between CO and CH_4 in a warm H_2 -rich atmosphere. The path from CO to CH_4 climbs over three energy barriers, the first between CO and formaldehyde (H_2CO), the second between formaldehyde and methanol (CH_3OH), and the third between methanol and methane. The three barriers can be thought of as reducing the $\text{C}\equiv\text{O}$ triple bond to a double bond, reducing the $\text{C}=\text{O}$ double bond to a single bond, and splitting C from O entirely.

In photochemistry the first barrier is unimportant because atomic hydrogen is generated in abundances that vastly exceed equilibrium (Liang et al. 2003). Kinetic barriers to adding H to CO to make HCO or adding H to HCO to make H_2CO are insignificant. The third barrier is unimportant in photochemistry because incident UV radiation readily splits CH_3OH into CH_3 and OH , which is quickly followed by adding photochemical H to CH_3 to make CH_4 . In photochemistry the energy to overcome the first and third barriers comes from UV photons.

By contrast, the middle barrier is not easily overcome by photochemistry. Formaldehyde is readily photolyzed but the products are either CO or HCO ; i.e., regress that leaves the $\text{C}=\text{O}$ bond unbroken. Meanwhile successive 3-body additions of photochemical H to H_2CO to make CH_3OH face considerable kinetic barriers, save at high temperatures where CH_4 is not favored. The historic focus of the planetary literature was therefore on reac-

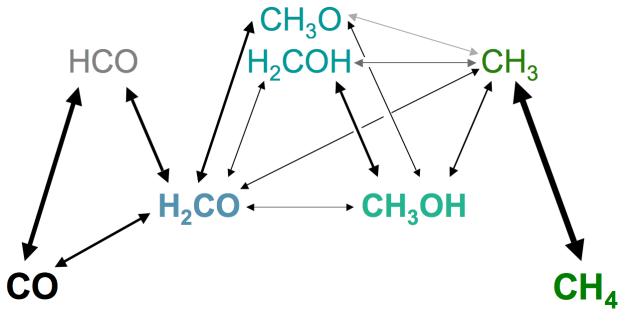


FIG. 1.— Major chemical pathways linking CO and CH₄ in an H₂-rich atmosphere. Reactions from left to right are with H₂ or H. Key intermediate molecules are formaldehyde (H₂CO) and methanol (CH₃OH). Other intermediates (HCO, H₂COH, CH₃O, CH₃) are short-lived free radicals. Where the species are plotted gives a rough indication of the energetics. Energy barriers correspond to breaking C-O bonds: from triple to double, from double to single, and from single to freedom. Relative magnitudes of reaction rates are indicated by arrow thickness for conditions near the quench point in a particular model (red star on Fig 4) that gives roughly equal amounts of CO and CH₄. At higher temperatures and lower pressures the plot as a whole would tilt to the left, with carbon pooling in CO. At lower temperatures and higher pressures the plot as a whole tilts to the right and carbon pools in CH₄. The energy barriers pose greater obstacles when the gas is colder.

tions that go from formaldehyde to methanol. Prinn and Barshay (1977) suggested $\text{H}_2 + \text{H}_2\text{CO} \rightarrow \text{CH}_3 + \text{OH}$, an ambitious reaction that jumps two hurdles at once, as the rate-limiting step, while Yung et al (1988) suggested that $\text{H} + \text{H}_2\text{CO} + \text{M} \rightarrow \text{CH}_3\text{O} + \text{M}$ (where M represents a third body) would be the bottleneck. Both schemes have been widely used, for Jupiter (Bézar et al. 2002), EGPs (Cooper and Showman 2006; Line et al. 2011), and BDs (Hubeny and Burrows 2007; Barman et al. 2011a).

Without the photochemical assist, any of the three barriers could potentially block the reaction. Recently, Moses et al. (2011) concluded that the rate-limiting reaction is the one that breaks the C-O single bond. They report that the bottleneck is between methanol and methane, $\text{CH}_3\text{OH} + \text{M} \rightarrow \text{CH}_3 + \text{OH} + \text{M}$ when methane is abundant, or goes through a free radical $\text{H} + \text{H}_2\text{COH} \rightarrow \text{CH}_3 + \text{OH}$ when methane is scarce. We will concur with the former but not the latter.

3. THE PHOTOCHEMICAL MODEL

Standard 1D codes simulate atmospheric chemistry by computing the gains and losses of chemical species at different altitudes while accounting for vertical transport. Vertical transport is parameterized as a diffusive process with an “eddy diffusion coefficient,” denoted K_{zz} [cm²/s]. Volume mixing ratios f_i of species i are obtained by solving continuity

$$N \frac{\partial f_i}{\partial t} = P_i - L_i N f_i - \frac{\partial \phi_i}{\partial z} \quad (1)$$

and force (flux)

$$\phi_i = b_{ia} f_i \left(\frac{m_a g}{kT} - \frac{m_i g}{kT} \right) - (b_{ia} + K_{zz} N) \frac{\partial f_i}{\partial z} \quad (2)$$

equations. In these equations N is the total number density (cm⁻³); $P_i - L_i N f_i$ represent chemical production

and loss terms, respectively; ϕ_i is the upward flux; b_{ia} , the binary diffusion coefficient between i and the background atmosphere a , describes true molecular diffusion; and m_a and m_i are the molecular masses of a and i . We implement molecular diffusion of a heavier gas through H₂ by setting $b_{ia} = 6 \times 10^{19} (T/1400)^{0.75} \text{ cm}^{-1} \text{ s}^{-1}$ —appropriate for CO—for all the heavy species. This is a reasonable approximation for present purposes, as our concern is with quenching at altitudes well below the homopause. The physical meaning of b_{ia} is the ratio of the relative thermal velocities of the two species to their mutual collision cross section. In the present circumstances, the relative thermal velocity is effectively that of H₂, so the only important source of variation in b_{ia} stems from the different diameters of the molecules. The code has been used by Zahnle et al. (2009) to address hot Jupiters and by Miller-Ricci Kempton et al. (2011) and Morley et al. (2013) to address H₂-rich hot Neptunes and super-Earths.

Temperature and pressure profiles are imported from the output of detailed radiative-convective models that are described elsewhere (Saumon & Marley 2008). The models are cloudless and of solar metallicity. Adding cloud opacity would make the p - T profiles hotter and less favorable to CH₄. The cloudless model is something of a best case for methane.

Treating vertical transport as diffusion is a necessary evil in a 1-D code. We will regard K_{zz} as a mildly constrained free parameter. In free convection, K_{zz} has been estimated from mixing length theory (Gierasch & Conrath 1985),

$$K_{zz} = \frac{1}{3} H \left(\frac{R_{\text{gas}} F_{\text{conv}}}{\mu \rho C_p} \right)^{1/3}, \quad (3)$$

where R_{gas} is the universal gas constant, F_{conv} the convective heat flux, μ the mean molecular weight (dimensionless), ρ the density, and C_p the heat capacity of the gas. The mixing length is approximated by the scale height. An upper bound is obtained from Eq 3 by equating F_{conv} with σT_{eff}^4 ,

$$K_{zz} < 2.5 \times 10^{10} \left(\frac{T_{\text{eff}}}{600} \right)^{8/3} \left(\frac{1000}{g} \right) \text{ cm}^2/\text{s}. \quad (4)$$

These large values of K_{zz} might be regarded with some skepticism. If applied to Earth’s troposphere, Eq 3 predicts $K_{zz} > 10^7 \text{ cm}^2/\text{s}$, which is two orders of magnitude too high. Even in the present context, F_{conv} can be much smaller than σT_{eff}^4 (or even fall to zero in places), because a considerable fraction of energy transport is by radiation. Depending on how well one tolerates theory, one might expect K_{zz} to be of the order of 10^9 - $10^{11} \text{ cm}^2/\text{s}^2$ in the convecting zones of self-luminous EGPs, and $100 \times$ smaller for BDs with $g = 10^5 \text{ cm}/\text{s}^2$.

It is likely that K_{zz} would be much smaller in stratified gas above the convecting regions. On Earth, K_{zz} drops by two orders of magnitude at the tropopause. Hubeny and Burrows (2007) reduce K_{zz} by several orders of magnitude in the stratosphere. Simulations by Freytag et al. (2010) support this expectation. The tradeoff is between simplicity (constant K_{zz}) and realism (a vertical discontinuity in K_{zz}). The latter choice would introduce two more free parameters, the value of K_{zz} in the strato-

sphere (ill constrained) and the altitude of the discontinuity (reasonably well constrained, but results could be sensitive to this). A two layer model also makes interpreting the numerical results in terms of a quench approximation less straightforward because there can be more than one quench point. For this study we choose to treat K_{zz} as constant with height, but vary it over a range wide enough to encompass all likely values.

The chemical system used here comprises 366 forward chemical reactions and 32 photolysis reactions of 64 chemical species made of H, C, N, O, and S. The most important missing species is probably methylamine, CH_3NH_2 . Reaction rates when known are selected from the publicly available NIST database (<http://kinetics.nist.gov/kinetics>). Although many of the important reactions have been measured in both directions in the lab (e.g., both $\text{CH}_4 + \text{H} \rightarrow \text{CH}_3 + \text{H}_2$ and $\text{CH}_3 + \text{H}_2 \rightarrow \text{CH}_4 + \text{H}$ have been heavily studied), in general one direction is much better characterized than the other. Thermodynamic data (enthalpies and entropies) are usually better known over a wider range of temperatures. Thus it is better to complement each specific reaction with its exact reverse, with the forward and reverse rates linked self-consistently by the thermodynamic data of the species involved. This way the transition from equilibrium to kinetically-controlled abundances is automatic. Equilibrium is reached when all the important forward and reverse reactions are fast compared to changes in the state variables.

How this is done is fully explained by Visscher and Moses (2011). What follows is a telegraphic summary. For reactions of the form $\text{A} + \text{B} \rightarrow \text{C} + \text{D}$ with forward reaction rate k_f , the reverse rate (i.e., the rate for $\text{C} + \text{D} \rightarrow \text{A} + \text{B}$) is $k_r = k_f \exp(-\Delta G/RT)$, where ΔG , the Gibbs free energy, is obtained from enthalpies and entropies of the of the reactants and products, $\Delta G = H_A + H_B - H_C - H_D - T(S_A + S_B - S_C - S_D)$. For associative reactions of the form $\text{A} + \text{B} \rightarrow \text{AB}$, the rate for the reverse reaction (dissociation of AB) is $k_r = k_f (kT/P_o) \exp(-\Delta G/RT)$, where $P_o = 10^6$ dynes/cm² is one atmosphere. Similarly, the associative reverse of a dissociative reaction is given by $k_r = k_f (P_o/kT) \exp(-\Delta G/RT)$.

Thermodynamic data as a function of temperature are available for atoms and most small molecules from NIST in the form of empirical Shomate equation fits for enthalpy and entropy (<http://webbook.nist.gov/chemistry/form-ser>). Zero point data for HS are corrected by Lodders (2004). For CH_3OH and C_2H_6 we use heat capacities as a function of temperature to derive Shomate equation fits for enthalpy and entropy. Unfortunately, many of the more exotic free radicals are not listed in the publicly available NIST databases. For many of these we use estimates given in Burcat and Ruscic (2005)'s widely available gray literature compilation. For NNH we follow Haworth et al. (2003), and for N_2H_2 and N_2H_3 we follow Matus et al. (2006). Inaccurate thermodynamic data for free radicals are not a problem for equilibrium calculations of well-characterized abundant species because poorly-characterized free radicals are never abundant. On the other hand, poorly-characterized species do pose a problem in disequilibrium kinetics because net reaction rates

depend on the uncertain abundances of free radicals, which are determined by their thermodynamic properties.

The lower boundary is set deep enough that all species are in thermodynamic equilibrium. We find that pressures above 300 bars and temperatures above 2000 K usually suffice, with the limiting species being N_2 . The upper boundary condition is zero flux for all species. We place the upper boundary at $\sim 10^{-6}$ bars, as higher altitudes require additional physics and chemistry (ion chemistry, thermospheric heating) that go beyond the scope of this work. Steady state solutions are found by integrating the time-dependent chemical and transport equations through time using an overcorrected fully implicit backward-difference method. Most models take a few minutes to run to steady state from arbitrary initial conditions on a vintage laptop computer, although some particular cases can be more challenging.

Photolysis significantly affects the composition of atmospheres at very high altitudes even when the incident UV flux is small. In our models we have set the incident UV flux to 0.1% that at Earth. Photolysis plays almost no part at the higher pressures germane to quenching and is not further discussed here. We have not included the reverses of photolysis reactions (radiative attachment, e.g. $\text{OH} + \text{H} \rightarrow \text{H}_2\text{O} + h\nu$) in detailed balancing. Recent work has shown that radiative attachment can be important in hydrocarbon growth in planetary atmospheres when the resulting molecule is complex enough that radiative relaxation can be effective (Vuitton et al. 2012).

3.1. Two examples

Figure 2 shows how K_{zz} effects chemistry on a tepid ($T_{\text{eff}} = 600$ K), cloud-free, relatively low mass ($g = 10^3$ cm/s²) extrasolar planet of solar composition. Insolation is insignificant. Three different K_{zz} are compared. (i) Strong vertical mixing— $K_{zz} = 10^{10}$ cm²/s—suppresses CH_4 and maintains $f_{\text{CO}} \gg f_{\text{CH}_4}$ to very high altitudes. CO and CH_4 are in chemical equilibrium below the quench point at ~ 4 bars and 1450 K. (ii) A more Jupiter-like $K_{zz} = 10^7$ cm²/s raises the quench point to 1.5 bars and 1280 K, which is better for CH_4 . (iii) Weak mixing, $K_{zz} = 10^4$ cm²/s, raises the quench point to 0.6 bars and 1000 K, which is cool enough, barely, to fall into the CH_4 field, so that $f_{\text{CH}_4} > f_{\text{CO}}$ in this planet's photosphere. The effect of molecular diffusion (in which heavy molecules sink through H_2) is apparent above 3×10^{-6} bars at $K_{zz} = 10^7$ cm²/s and above 3×10^{-3} bars at $K_{zz} = 10^4$ cm²/s.

At a given effective temperature, surface gravity determines whether the atmosphere is CO or CH_4 dominated. Figure 3 shows CO and CH_4 abundances in three worlds that differ only in their surface gravities. The atmospheres are cloud-free and of elementally solar composition. The models shown here have effective radiating temperatures of 600 K and a Jupiter-like $K_{zz} = 10^7$ cm²/s. Surface gravities range from a Saturn-like $g = 10^3$ cm/s² to a brown-dwarf-like $g = 10^5$ cm/s². The computed CO/ CH_4 ratio is sensitive to surface gravity. This is because the p - T profile is displaced to higher pressures and lower temperatures when gravity is higher. Quenching at higher pressures and lower temperatures favors CH_4 over CO. The result is that the 600 K planet

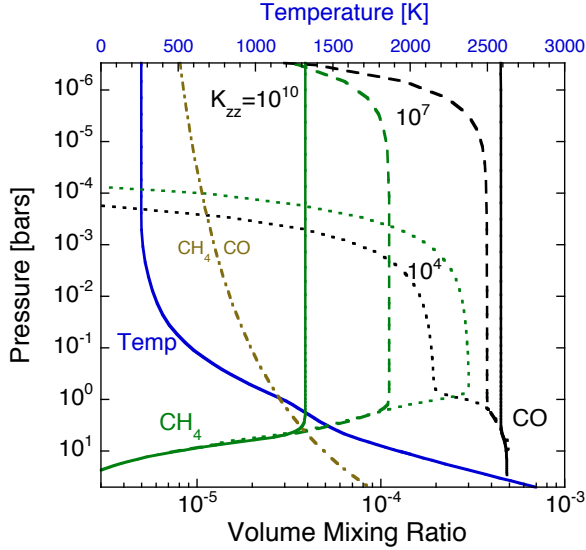


FIG. 2.— Methane and CO in an exemplary lukewarm EGP. The planet is cloud-free, has an effective radiating temperature of 600 K, $g = 10^3$ cm/s², and receives insignificant insolation. The p - T profile of the atmosphere is compared to the p - T curve (gold dot-dash) corresponding to equilibrium $f_{\text{CH}_4} = f_{\text{CO}}$. Methane is thermodynamically favored when T is to the left of the $f_{\text{CH}_4} = f_{\text{CO}}$ curve, CO is favored to the right. Computed CO and CH₄ mixing ratios are shown from three 1D kinetics models that differ only in vertical eddy mixing: $K_{zz} = 10^{10}$ cm²/s (solid), $K_{zz} = 10^7$ cm²/s (dashed), and $K_{zz} = 10^4$ cm²/s (dots). Deep in the atmospheres CO and CH₄ are in equilibrium. High in the atmospheres CO and CH₄ are unreactive and f_{CO} and f_{CH_4} would be constant but for molecular diffusion. The quench points are obvious and well-defined in all three models.

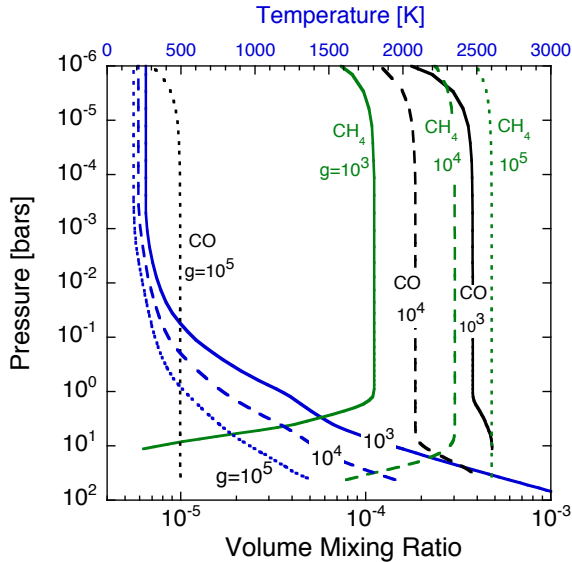


FIG. 3.— Three models with three different surface gravities. The plot shows p - T profiles and CO and CH₄ abundances. The planets are 600 K, self-luminous, cloudless, of solar composition, with $K_{zz} = 10^7$ cm²/s. Surface gravities are $g = 10^3$ cm/s² (solid), $g = 10^4$ cm/s² (dashed), and $g = 10^5$ cm/s² (dots). Higher gravity models are colder at a given pressure and are more favorable to CH₄.

($g = 10^3$ cm/s²) has abundant CO and relatively little CH₄, while the 600 K brown dwarf is methane-rich with only a trace of CO.

3.2. The ensemble of models

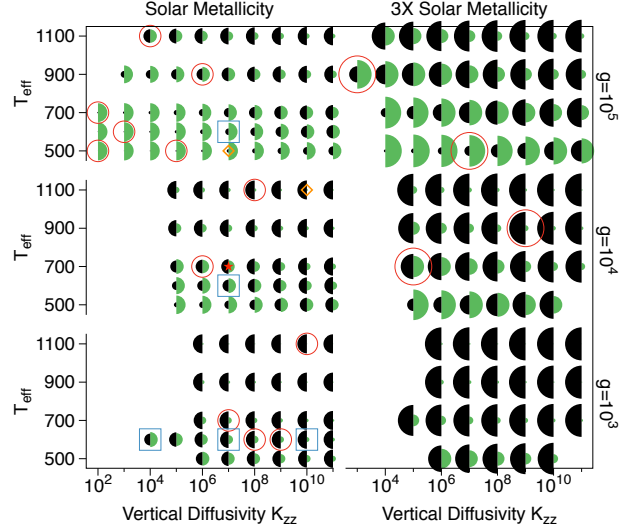


FIG. 4.— An overview of the ensemble of models. There are six panels for six different combinations of gravity and metallicity. Relative CO and CH₄ abundances above the quench point are indicated by the areas of the semicircles, CO black and following, CH₄ green and preceding. In general, higher gravities, cooler temperatures, and lower metallicity favor CH₄ vs. CO. Different metallicities can give the same CO/CH₄ ratio at the same T_{eff} and g with modest and probably unmeasurable differences in K_{zz} . Blue squares denote the 16 cases used in Fig 7 to illustrate quenching. Red circles denote the two models used in Fig 8 to compare reaction rates. The red star is the guide to Fig 1. In all cases, equilibrium $f_{\text{CH}_4} > f_{\text{CO}}$.

We use the 1D chemical kinetics models to explore the phase space defined by $500 < T_{\text{eff}} < 1100$ K, $10^4 < K_{zz} < 10^{11}$ cm²/s, and $10^3 < g < 10^5$ cm/s². Models are run to steady state. Ensembles were computed at solar ($m = 1$) and thrice solar ($m = 3$) metallicities, but p - T profiles were not adjusted to take into account the altered chemical composition. The CO and CH₄ abundances of all the models are summarized in Figure 4. Low K_{zz} models can be numerically challenging when the gas is very hot. We include two models that did not reach a true steady-state on Figure 4: $T_{\text{eff}} = 600$ K, $g = 10^3$ cm/s², $m = 1$, and $K_{zz} = 10^4$ and 10^5 cm²/s. These models reached persistent near steady states, but were held back by undiagnosed features in the sulfur chemistry. They are included here as part of our exploration of conditions that can produce CH₄ at low gravity.

4. DETERMINING THE QUENCH POINT FOR CO AND CH₄

Here we want to determine the quench conditions that correspond to the asymptotic CO and CH₄ abundances in the complete kinetics models shown in Figure 4. Our purpose in doing so is to quantify the emergent quench behaviour of the kinetics models, and if possible describe

this behaviour with a simple equation or set of equations. That it is possible to do this is the subject of Figure 5.

First, we determine the CO-CH₄ quench point in each atmosphere in Figure 4 by finding the lowest altitude in each atmosphere where the CO and CH₄ mixing ratios depart measurably from equilibrium. Deep in the atmosphere CH₄ and CO are in chemical equilibrium with H₂ and H₂O. Thus the product

$$K_{\text{test}} = \frac{p\text{CH}_4 \cdot p\text{H}_2\text{O}}{p\text{CO} \cdot (p\text{H}_2)^3} \quad (5)$$

equals the corresponding equilibrium constant

$$K_{\text{CH}_4\text{-CO}} = 5.24 \times 10^{-14} \exp(27285/T). \quad (6)$$

In Eqs 5 and 6 (and all succeeding expressions of similar form), pressures are in atmospheres and temperatures in Kelvins.

In the regions of a convective atmosphere relevant to the present investigation, equilibrium contours of constant CH₄/CO are always shallower than the adiabat, hence the equilibrium CH₄ mixing ratio always decreases with increasing depth. To show this (and its limits), use the adiabatic relation $T^\gamma \propto p^{\gamma-1}$, where $\gamma = C_p/C_v$ has its usual meaning as the ratio of heat capacities. The temperature gradient along the adiabat (constant entropy S) is

$$\left(\frac{\partial T}{\partial p}\right)_S = \frac{\gamma - 1}{\gamma} \frac{T}{p} = \frac{R}{C_p} \frac{T}{p}. \quad (7)$$

For a temperate cosmic mix of H₂ (84%) and He (16%), we can expect H₂ to have $C_p \approx 3.5R$ and He to have $C_p = 2.5R$, and hence $R/C_p \approx 0.30$. Warmer temperatures excite hydrogen's vibrational modes, for which $C_p \approx 4.5R$ and $R/C_p \approx 0.24$. Detailed calculations show that R/C_p decreases monotonically from 0.29 at 1000 K to 0.25 at 2100 K to 0.20 at 3000 K as dissociation (another energy sink) becomes important.

Equation 7 needs to be compared to contours of equilibrium chemistry. Defining $\xi \equiv \text{CH}_4/\text{CO}$, we can write the equilibrium (Eqs 5 and 6) in the form

$$\xi \cdot \left(f_{\text{O}} - \frac{f_{\text{C}}}{1 + \xi}\right) = p^2 f_{\text{H}_2}^3 A e^{B/T} \quad (8)$$

where $f_{\text{H}_2} \approx 0.84$ is the H₂ mixing ratio, $f_{\text{O}} \approx f_{\text{H}_2\text{O}} + f_{\text{CO}}$ is the total oxygen mixing ratio, and $f_{\text{C}} \approx f_{\text{CH}_4} + f_{\text{CO}}$ is the total carbon mixing ratio. These are generally very good approximations for $T < 2500$ K. The quantity in parentheses is $f_{\text{H}_2\text{O}}$. For contours of constant ξ , the left hand side of Eq 8 is constant. Taking derivatives, the temperature gradient is

$$\left(\frac{\partial T}{\partial p}\right)_\xi = \frac{2T}{B} \frac{T}{p} \approx 0.11 \frac{T}{1500} \frac{T}{p}. \quad (9)$$

Thus $(\partial T/\partial p)_\xi < (\partial T/\partial p)_S$ for temperatures lower than about 2900 K, by which point several of the assumptions made in deriving this relation have begun to break down. Even with K_{zz} as high as 10^{11} cm²/s, quenching in the CO-CH₄ system takes place at temperatures less than 2200 K. Hence we can always presume that CO is most abundant and CH₄ least abundant at the lower

boundary of our model. It follows that we can determine the quench conditions (temperature T_q , pressure p_q) by working up from the lower boundary and finding the lowest altitude at which the product K_{test} is appreciably smaller than the equilibrium constant $K_{\text{CH}_4\text{-CO}}$. In practice we searched for the lowest altitude where $K_{\text{test}} < 0.9K_{\text{CH}_4\text{-CO}}$.

We also wish to determine a quench timescale t_q . In principle, the right way to do this is to determine the true chemical reaction timescale from the sum of all relevant reaction rates at the quench point. In general this information is surprisingly hard to extract from a model, because the breakdown of equilibrium appears as small differences between much larger forward and reverse reaction rates in many reactions. This approach is practical only if one already knows exactly which species and reactions are key. Once known, for t_q to be useful in a quench approximation one then needs a comparably fine-grained description of the cooling time implicit in K_{zz} and the particular chemical reactions that establish t_q .

Much easier, and more useful, is to define a quench timescale for the system as a whole in terms of a relevant mixing time, $t_q = t_{\text{mix}} = L^2/K_{zz}$ where L is a characteristic length scale. The simple choice is to set $L = H_q$, the scale height at T_q . This definition is arbitrary to within a multiplicative factor because the true mixing length L is not in general equal to H_q . But this definition of t_q is precisely what is needed for constructing a new quench approximation that assumes $t_{\text{mix}} = H_q^2/K_{zz}$ and, as seen in Figure 5, it leads to a very simple description of the overall behaviour of the full network of chemical reactions.

Smith (1998) demonstrated that L is often considerably shorter than H , mostly because the key reactions determining t_q are much more sensitive to temperature than to pressure. Smith (1998) developed a five step iterative algorithm for determining L and presented it in the form of a ‘‘recipe’’ to be used in quenching calculations, which is especially useful when the system is controlled by a single reaction whose rate is known. Several workers have employed Smith's recipe. Unfortunately, the range of mixing times that results can be very great. For example, Visscher and Moses (2011) list values for L between $0.1H$ and $0.7H$ for the CO-CH₄ system, the equivalent of a factor of 50 in t_{mix} and therefore equivalent to a factor of 50 in the inferred value of K_{zz} , itself a parameter of easy virtue. The resulting uncertainty frustrates intercomparison between models. Our position is that the most useful approximations are simple approximations. We therefore stick with the old rule $L = H$ to define t_{mix} , rather than iterate between L and T_q . How L is defined is important for comparing to previous work that tries to estimate t_{chem} from particular reaction rates, but it is simply a scaling factor for us.

Irrespective of how L is defined, we find that we can fit the quench time t_q to a simple functional form that spans all our models. We start from the expectation that CO \rightarrow CH₄ will depend on temperature and pressure, perhaps the C/O ratio, and possibly on metallicity. It is reasonable to hope that the net reaction has an Arrhenius-like rate

$$t_q = A p^{-b} m^{-c} \exp(B/T), \quad (10)$$

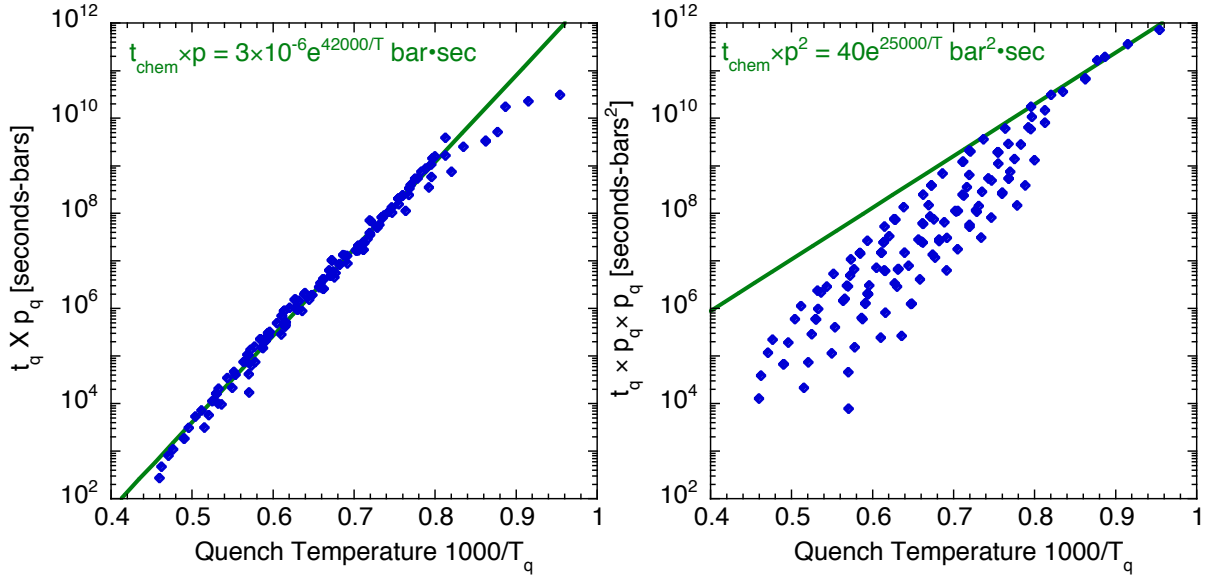


FIG. 5.— CO-hydrogenation timescales as a function of quench point temperature T_q and quench pressure p_q for the ensemble of solar composition kinetics models. Quench conditions T_q and p_q are determined numerically from the full kinetics models using the entire network of chemical reactions. How this is done is explained in the text. The quench timescale used here is a mixing timescale, $t_q = t_{\text{mix}} \equiv H_q^2/K_{zz}$, where H_q is the pressure scale height at the quench point. The relation between the true chemical timescale and t_q is arbitrary to a factor L^2/H_q^2 , where L refers to the true mixing length. We do not plot t_q itself (for which the points are scattered), but rather $t_q \times p_q$ (left) and $t_q \times p_q^2$ (right), which resolve into orderly arrays. *Left.* A simple exponential provides a good fit to $t_q \times p_q$ for all but the coldest T_q . *Right.* A different simple exponential can be fit to $t_q \times p_q^2$ for the coldest T_q . Lines show fits.

where possible pressure and metallicity dependencies are written as power laws.

Our hope is nicely borne out by Figure 5, which plots t_q for the CO-CH₄ reaction for our complete roster of solar metallicity models. All but the coldest quench points are described by a rather well-defined Arrhenius expression with $b=1$. The Arrhenius fit (for $m=1$) is

$$t'_{q1} = 3.0 \times 10^{-6} p^{-1} \exp(42000/T) \text{ sec}, \quad (11)$$

where p is in bars. The time scale for models with $m=3$ (not shown) is roughly half of this.

The prime is placed on t'_{q1} because, by using $K_{\text{test}} < 0.9K_{eq}$ rather than $K_{\text{test}} < K_{eq}$, we have overestimated the quench time. To correct for this—and to verify that a quench scheme works—we compare the predictions of the quench scheme with the predictions of the ensemble of models. Fits are shown in Figure 6. These use

$$t_{q1} = 1.5 \times 10^{-6} p^{-1} m^{-0.7} \exp(42000/T) \text{ sec}. \quad (12)$$

The methods of Figure 6 and Figure 5 are complementary. A satisfactory fit on Figure 6 is more sensitive to the A factor (overall rate) and the metallicity (Eq 10), whilst the fit on Figure 5 is more sensitive to the B factor (temperature dependence) and pressure.

The half-dozen models that are ill fit by Eq 11 are fit instead by a second Arrhenius relation

$$t_{q2} = 40 p^{-2} \exp(25000/T) \text{ sec}. \quad (13)$$

where we have given the iterated rate. The models fit by Eq 13 are those with very low quench temperatures T_q and very little CO. We have no such models with $m=3$.

The high and low temperature fits combine harmonically to give a general description of reaction times in

the CO-CH₄ system,

$$t_{\text{CO}} = \left(\frac{1}{t_{q1}} + \frac{1}{t_{q2}} \right)^{-1}. \quad (14)$$

Equation 14 when used with the timescale $t_{\text{mix}} = H^2/K_{zz}$ works for all of our models for CO and CH₄ and we expect should work generally for compositions not too far from solar.

4.1. Analysis

We examine the ensemble of models for quench points pertinent to the reaction intermediates, to determine where in the CO-CH₄ reaction network quenching first takes place. We consider the CO-H₂CO, H₂CO-CH₃OH, and CH₃OH-CH₄ equilibria. We analyzed 16 models taken arbitrarily from the ensemble. The chosen ones are marked on Fig 4 with scarlet circles. We find, to within our ability to determine this, that the CH₃OH-CH₄ reaction quenches at the same temperature as the CO-CH₄ reaction as a whole. This is shown by panels (c) and (d) of Figure 7. By contrast the CO-H₂CO and H₂CO-CH₃OH reactions stay near equilibrium for temperatures above 900 K (Figures 7a and 7b). Hence as a parcel cools equilibrium first breaks down between CH₃OH and CH₄. This is in accord with conclusions reached by Moses et al. (2011) and Visscher and Moses (2011).

Figure 8 examines in detail the key reactions that break the CO-CH₄ equilibrium. The important reactions form the methyl radical CH₃ from species such as CH₃OH in which the C-O bond is still intact. Figure 8 illustrates two cases, one a cool ($T_{\text{eff}} = 500$ K) brown dwarf with a preference for CH₄ ($f_{\text{CO}} = 1.4 \times 10^{-5}$, $f_{\text{CH}_4} = 4.7 \times 10^{-4}$), the other a warmer ($T_{\text{eff}} = 1100$ K), smaller world that

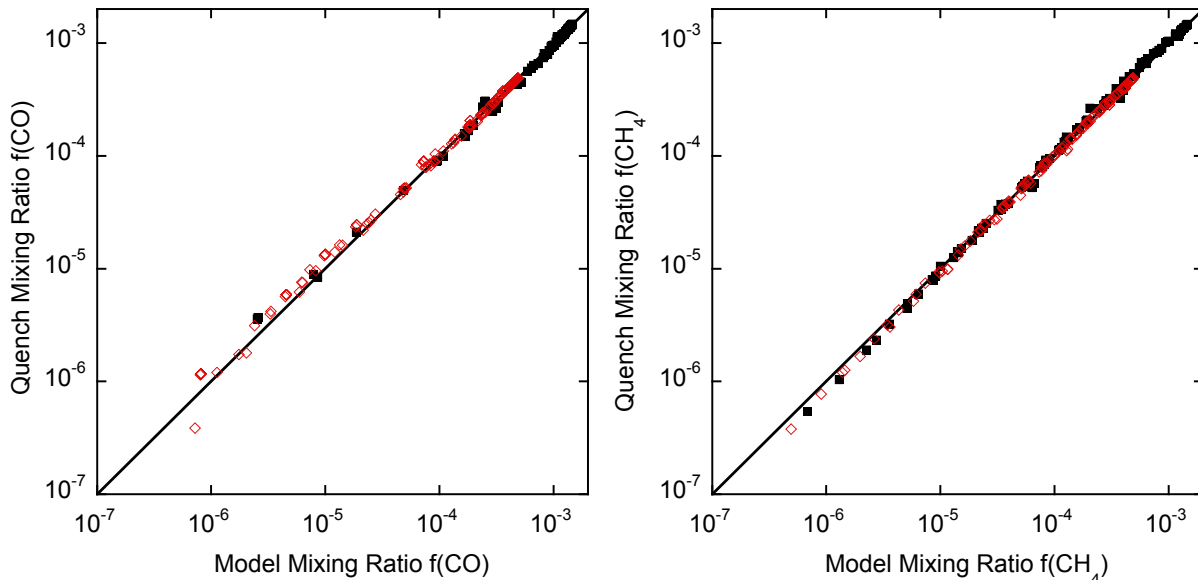


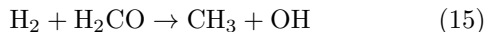
FIG. 6.— CO (left) and CH₄ (right) mixing ratios predicted by the quenching approximation $t_{\text{chem}} = t_{\text{mix}}$ (y-axis) plotted against the actual asymptotic mixing ratio determined from the full ensemble of 1-D kinetics model (x-axis). A perfect approximation would adhere to the line. Open red symbols are for $m=1$ and solid black symbols are for $m=3$ using Eq 12.

favors CO ($f_{\text{CO}} = 4.8 \times 10^{-4}$, $f_{\text{CH}_4} = 1.0 \times 10^{-5}$). Both models assume solar metallicity ($m = 1$). In both cases the most important reaction is simple thermal decomposition of methanol, $\text{CH}_3\text{OH} + \text{M} \rightarrow \text{CH}_3 + \text{OH}$, although the reaction of methanol with atomic hydrogen is nearly as fast in the colder, higher gravity case. The reaction $\text{H}_2\text{COH} + \text{H}$, which Moses et al. (2011) report as the most important in their CO-rich models, does not appear to be very important in ours. We do not claim that our system is better; we merely point out that abundances and reaction rates of furtive species like H_2COH are highly uncertain.

4.2. Comparisons with previous work

To put our results in perspective, we compare them to some quench approximations seen in the literature. Published quench approximations begin by identifying a particular forward reaction as the bottleneck and then calculate CO loss time scales from the chosen reaction’s rate; variety lies in the reactions that are chosen and the reaction rates adopted.

We begin with the classic Prinn and Barshay (1977) prescription, used by Hubeny and Burrows (2007) as their “slow” case. Prinn and Barshay (1977) suggested



as a rate-limiting reaction, with reaction rate $k_f = 2.3 \times 10^{-10} e^{-36200/T} \text{ cm}^3/\text{s}$. R15 is a reaction that jumps over two energy barriers in Figure 1, which makes it look like it should be relatively unlikely. Figure 8 shows that R15 is modestly important in our system, but we use a newer slower rate estimated by Jasper et al (2007). The time constant for CO loss by reaction R15 using Prinn and Barshay (1977)’s rate is approximated by the forward reaction

$$t_{\text{chem}}^{-1} = \frac{-1}{[\text{CO}]} \frac{\partial [\text{CO}]}{\partial t} = \frac{k_f [\text{H}_2] [\text{H}_2\text{CO}]}{[\text{CO}]} \text{ sec}^{-1} \quad (16)$$

where the notation $[\text{CO}]$ refers to number density [cm^{-3}].

To evaluate t_{chem} for R15, we put formaldehyde in equilibrium with CO and H₂,

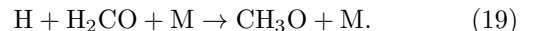
$$\frac{p_{\text{H}_2\text{CO}}}{p_{\text{H}_2} \cdot p_{\text{CO}}} = K_{\text{H}_2\text{CO}} = 3.3 \times 10^{-7} \exp(1420/T), \quad (17)$$

to obtain

$$t_{\text{chem}} = \frac{1.3 \times 10^{16} \exp(34780/T)}{p N f_{\text{H}_2}^2} \text{ sec}. \quad (18)$$

The number density N is related to the pressure p in bars by $NkT = 10^6 p$. The predictions of Eq 18 are compared to results from our complete models in Figure 9. Equation 18 works quite well in a quench approximation to our full model, especially for cases where CH₄ is predicted to be abundant, despite its being based on the wrong reaction with the wrong rate. As the Prinn and Barshay (1977) approximation has been widely used for a very long time, it is valuable to see that it seems to work rather well. When compared to Eq 12, Eq 18 has a stronger pressure dependence (p^{-2} vs. p^{-1}), a weaker temperature dependence ($T \cdot e^{34780/T}$ vs. $e^{42000/T}$), and no dependence on metallicity.

More recent discussions of the CO-CH₄ quench approximation omit enough details that they can be challenging to reproduce. We attempt to do so here because the comparisons are illuminating. Yung et al. (1988) suggested that the rate-limiting step is the 3-body reaction



Hubeny and Burrows (2007) use R19 as their “fast” rate with $L = H$. Barman et al. (2011a) also use this rate, but following Smith (1998) they set the mixing length L to unspecified values between 10% to 20% of the scale height, which effectively slows the “fast” rate by a factor of 25-100 compared to $L = H$. Cooper and Showman (2006) implemented the CH₃O channel with a different reaction rate while following Smith’s “recipe.” We use the asymptotic high pressure rate

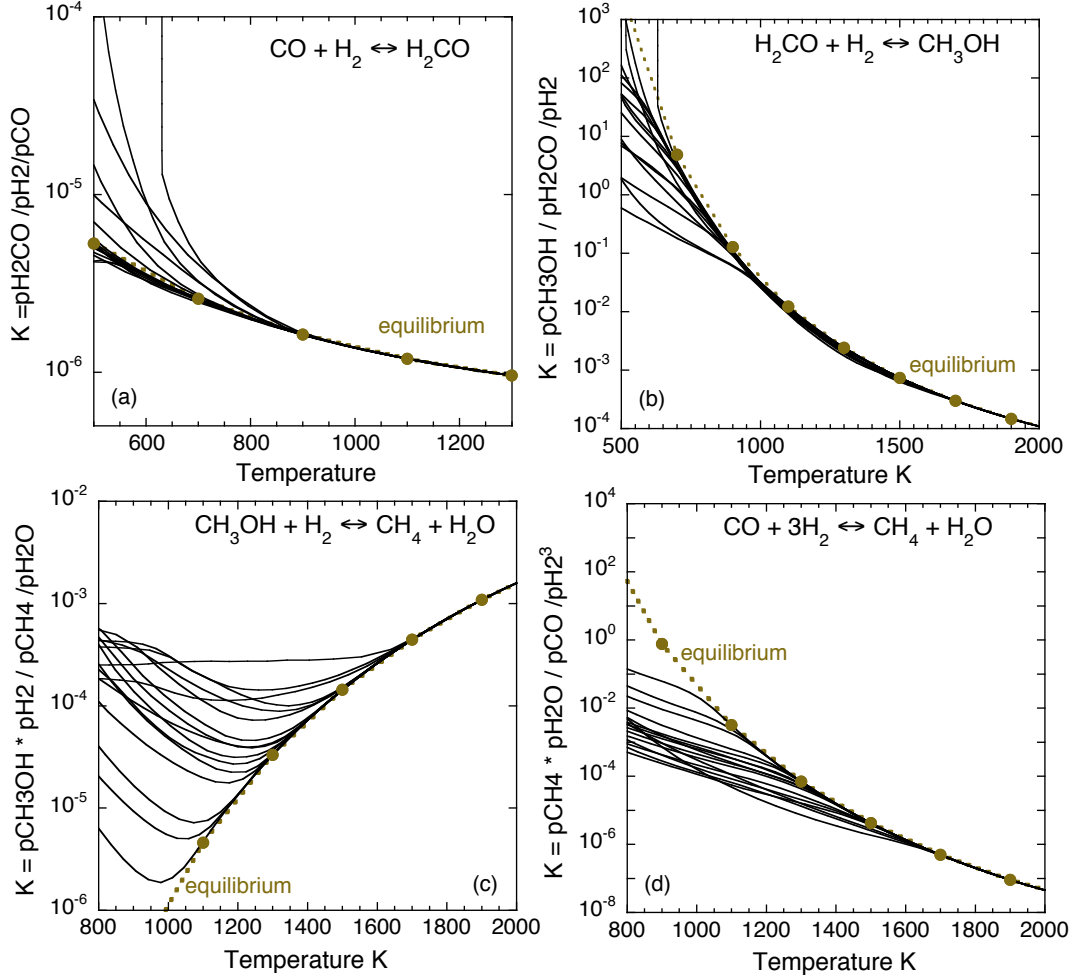


FIG. 7.— Quenching behavior of the three intermediate reactions (a, b, c) and of the $\text{CO} \leftrightarrow \text{CH}_4$ system as a whole (d). Results are shown from 16 models chosen to provide a representative sample of the ensemble (marked by red circles in Fig. 4). Panels (a,b) show that $\text{CO} \leftrightarrow \text{H}_2\text{CO}$ and $\text{H}_2\text{CO} \leftrightarrow \text{CH}_3\text{OH}$ appear to be equilibrated in all models at $T > 900$ K. Panel (c) shows that equilibration of CH_3OH and CH_4 is more difficult. In detail the quench points for $\text{CH}_3\text{OH} \leftrightarrow \text{CH}_4$ appear to be the same as the quench points for $\text{CO} \leftrightarrow \text{CH}_4$ as shown in panel (d) for the same 16 models. Evidently the bottleneck is between CH_3OH and CH_4 , in accord with conclusions reached by Moses et al (2011).

$$k_\infty = 8.0 \times 10^{-10} \exp(-3160/T),$$

a very fast rate which we obtained by reversing the first order rate for $\text{CH}_3\text{O} \rightarrow \text{H} + \text{H}_2\text{CO}$ given by Rauk et al. (2003). If we presume that H and H_2CO are both in equilibrium, we can use the hydrogen equilibrium constant $K_{\text{H},\text{H}_2} = 1155 e^{-26916/T} = p\text{H} \cdot p\text{H}_2^{-0.5}$ to obtain

$$t_{\text{chem}}^{-1} = \frac{k_\infty [\text{H}][\text{H}_2\text{CO}]}{[\text{CO}]} = k_\infty p^{1.5} f_{\text{H}_2}^{1.5} \left(\frac{10^6}{kT} \right) K_{\text{H}_2\text{CO}} K_{\text{H},\text{H}_2}. \quad (20)$$

Evaluated,

$$t_{\text{chem}} = 4.5 \times 10^{-10} T p^{-1.5} f_{\text{H}_2}^{-1.5} \exp(28656/T). \quad (21)$$

Results of using Eq 21 are shown as red diamonds on Fig 9 with $L = 0.14H$, which is comparable to what Barman et al. (2011a) use (the fit would look worse with $L = H$). These stand out with too much CH_4 and too little CO , because R19 is not a true bottleneck.

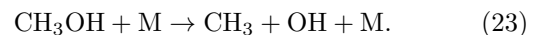
Line et al. (2011) moved the bottleneck to $\text{CH}_3\text{O} + \text{H}_2 \rightarrow \text{CH}_3\text{OH} + \text{H}$. To compute a rate constant, we use $p\text{CH}_3\text{O} = K_{\text{CH}_3\text{O}} \cdot p\text{H}_2 \cdot p\text{H} \cdot p\text{CO}$, where $K_{\text{CH}_3\text{O}} =$

$3.0 \times 10^{-11} e^{10582/T}$ is the relevant equilibrium constant (the large number of significant digits in these equilibrium constants do not imply accuracy). To complete the equation we also assume that H and H_2 are in equilibrium. We use the reaction rate given by Line et al. (2011), which results in

$$t_{\text{chem}} = \frac{1.2 \times 10^{29} \exp(45720/T)}{T^4 N p f_{\text{H}_2}^2} \text{ sec}. \quad (22)$$

Results are shown as green squares on Figure 9 using $L = H$, as Line et al. (2011) do. Because it predicts too much CO and too little CH_4 , t_{chem} given by Eq 22 is too slow.

Based on detailed analysis of the reactions in a complete 1D model similar to our own, Moses et al. (2011) concluded that the bottleneck is associated with breaking the C-O bond. They propose several key channels. One channel is thermal decomposition of methanol,



Visscher and Moses (2011) and Moses et al. (2011) state

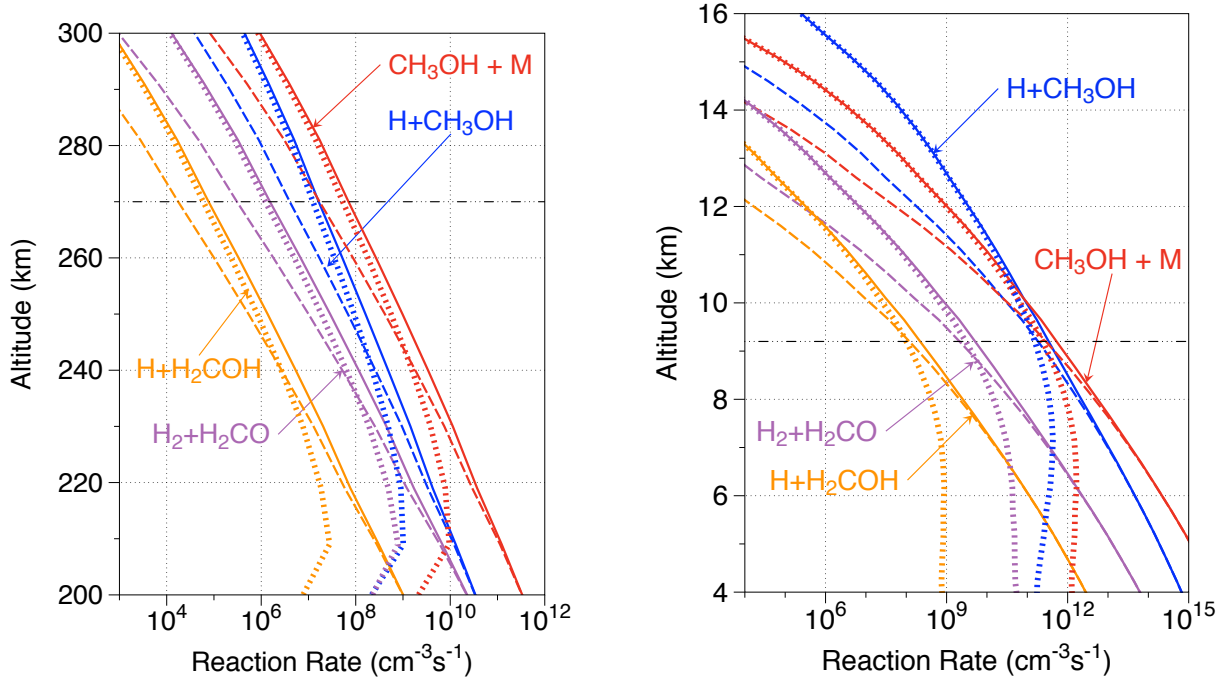


FIG. 8.— The four most important reactions for quenching in our model CO-CH₄ system. All four reactions yield CH₃ + OH as products. Solid curves show rates of the forward reaction that creates CH₃, dashed curves show the reverse reaction that destroys CH₃, and wide dots the difference (the net production of CH₃), which is equivalent to net loss of CO. Black dot-dash lines are the altitudes where CH₄ and CO reach their final quenched values. *Left*: A warm, strongly-mixed ($T_{\text{eff}}, K_{zz}, g = 1100, 10^{10}, 10^4$), model dominated by CO. Disequilibrium reactions are fastest at 210 km (at 1700 K) but full quenching is delayed until 270 km (at 1360 K); the distance corresponds to a bit more than a pressure scale height. *Right*: A cool, moderately-mixed ($T_{\text{eff}}, K_{zz}, g = 500, 10^7, 10^5$) BD dominated by CH₄. Disequilibrium reactions are fastest at 7 km but quenching is at 9 km (the scale height is 5 km).

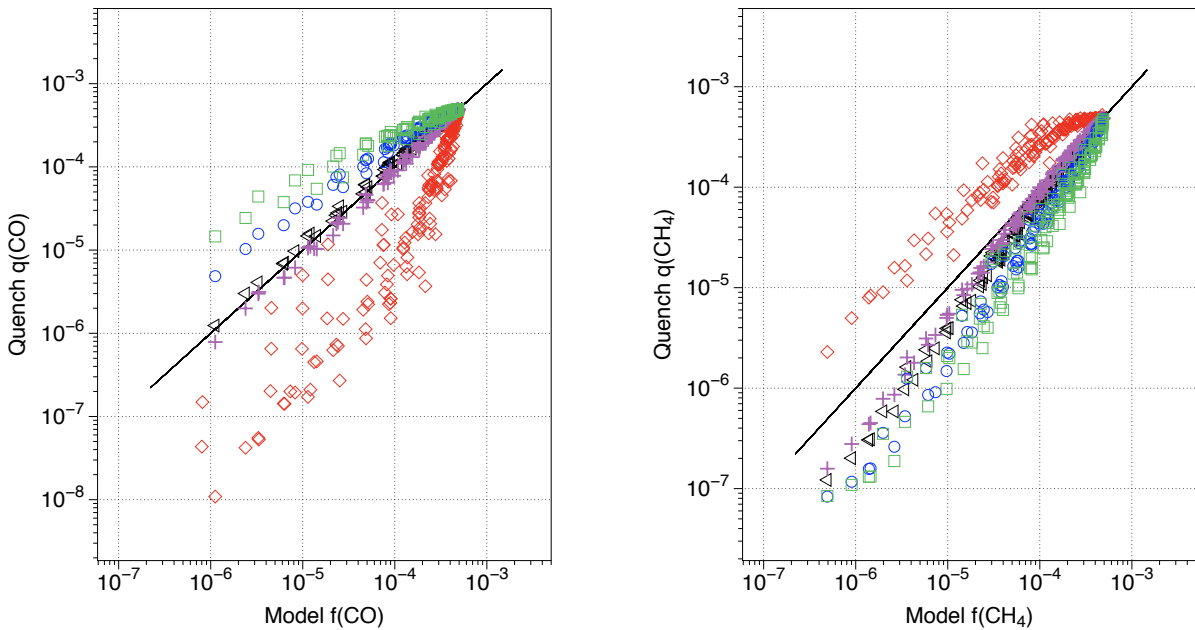
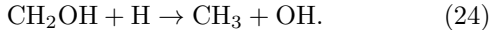


FIG. 9.— Comparison of some quench approximations (y-axes) to the actual CO and CH₄ mixing ratios computed by the full 1D model (x-axes). A perfect approximation would adhere to the line. Only results for solar metallicity ($m = 1$) are shown. Purple pluses follow the widely applied Prinn and Barshay (1977) model with $L = H$. Red diamonds use the channel through CH₃O suggested by Yung et al. (1988) but using a more recent estimate for the reaction rate and reducing the mixing length to $L = 0.14 H$; this is not the same as Yung et al. (1988)'s algorithm. Green squares implement Line et al. (2011)'s CH₃O channel with $L = H$. Black triangles implement the methanol decomposition channel favored for low f_{CO} by Moses et al. (2011) and Visscher and Moses (2011). These are computed with mixing length $L = 0.14 H$. Blue circles represent our attempt to implement the Moses et al. (2011) H₂COH channel with $L = 0.14 H$.

$\text{CO} \gg \text{CH}_4$, is



The rate of R24 depends on the uncertain thermodynamic properties of CH_2OH . In the high pressure limit, methanol decomposition R23 is a first order reaction,

$$\frac{\partial [\text{CH}_3\text{OH}]}{\partial t} = -k_\infty [\text{CH}_3\text{OH}]. \quad (25)$$

Jasper et al (2007) estimate k_∞ from theory

$$k_\infty = 6.251 \times 10^{16} (300/T)^{0.6148} \exp(-46573/T) \text{ sec}^{-1}.$$

The methanol equilibrium constant

$$K_{\text{CH}_3\text{OH}} = \frac{p_{\text{CH}_3\text{OH}}}{p_{\text{CO}} \cdot p_{\text{H}_2}} = 1.1 \times 10^{-13} e^{13000/T}$$

relates $[\text{CH}_3\text{OH}]$ to $[\text{CO}]$. The reaction timescale is then

$$t_{\text{chem}} = (k_\infty p_{\text{H}_2}^2 K_{\text{CH}_3\text{OH}})^{-1} \\ = 4.4 \times 10^{-6} T^{0.6148} \exp(33573/T) p^{-2} f_{\text{H}_2}^{-2} \text{ sec} \quad (26)$$

Equation 26 has a weaker dependence on T , a stronger dependence on p than we find for the ensemble, and no dependence on metallicity.

Figure 9 illustrates quenching using Eq 26 as black triangles. For the comparison we take $L = 0.14 H$. This approximates what Moses et al. (2011) may be using. Equation 26 does well, especially in cases where $\text{CO} \ll \text{CH}_4$ at quenching, which is the regime for which Moses et al. (2011) report that Eq 26 applies. Equation 26 does better if $L > 0.14 H$. The match is best for CO with $L = 0.2 H$, and better for CH_4 with $L \approx 0.5 H$.

To reconstruct a simple form for the H_2COH channel, we need to estimate the equilibrium abundance of H_2COH . We use $p_{\text{H}_2\text{COH}} = K_{\text{H}_2\text{COH}} \cdot p_{\text{H}_2} \cdot p_{\text{H}} \cdot p_{\text{CO}}$ with $K_{\text{H}_2\text{COH}} = 1.0 \times 10^{-12} e^{15843/T}$. We assume that H and H_2 are in equilibrium. Jasper et al. (2007) list a fast rate, $k = 2.8 \times 10^{-10} \text{ cm}^3/\text{s}$, for the reaction of H and H_2COH . Assembling the parts, we obtain

$$t_{\text{chem}} = \frac{2.7 \times 10^{15} \exp(38000/T)}{N p f_{\text{H}_2}^{-2}} \text{ sec}. \quad (27)$$

Results are shown as blue circles on Figure 9. Equation 27 has a similar T dependence to what we find for the system as a whole, but the overall rate is about 3 orders of magnitude slower using $L = 0.14 H$, or about ten times slower using $L = H$.

Disagreement between our model and Moses et al over the H_2COH channel is also apparent in Figure 8. The H_2COH radical plays a much more modest role in our 1-D code than it does in Moses et al. (2011)'s. The same is true for CH_3O . Why this should be so is likely related to differing guesses of H_2COH 's and CH_3O 's ill-known thermodynamic properties.

There are some more subtle differences between our model and previous quench models that should be noted. One is that we find $t_{\text{chem}} \propto p^{-1}$ by fitting to the ensemble, whilst quench models that attempt to identify the one key forward reaction tend to get $t_{\text{chem}} \propto p^{-2}$. This difference is the reason why quench prescriptions in Figure 9 that do well with $f_{\text{CO}} \ll f_{\text{CH}_4}$ miss the mark

somewhat with $f_{\text{CH}_4} \ll f_{\text{CO}}$. Figure 6 that uses $t_q \propto p^{-1}$ shows fine agreement at both ends of the scale.

Another difference is that we see a well-defined metallicity dependence when fitting to the ensemble. The metallicity dependence probably stems from the reverse reaction, which as noted is usually ignored. As equilibrium breaks down, the reaction slows in both directions, more quickly in the reverse direction than in the forward direction. This behavior is shown clearly in Figure 8, where forward, reverse, and net reaction rates are plotted. It is the net reaction, the difference between the forward and reverse reactions, that defines the retreat from equilibrium, not the forward reaction alone. For example, the time scale for the methanol decomposition channel is

$$t_{\text{net}}^{-1} = \frac{-1}{[\text{CO}]} \frac{\partial [\text{CO}]}{\partial t} = \frac{k_f [\text{CH}_3\text{OH}]}{[\text{CO}]} - \frac{k_r [\text{CH}_3] [\text{OH}]}{[\text{CO}]} \quad (28)$$

The reverse reaction is quadratic in metallicity, whilst $[\text{CO}]$ is quadratic in metallicity only for $f_{\text{CO}} \ll f_{\text{CH}_4}$, which suggests that it is through the reverse reaction that metallicity enters t_{CO} . The same consideration applies for all the important reactions in Figure 8, as the reverse reaction in every case is between CH_3 and OH.

5. QUENCHING IN THE N_2 - NH_3 SYSTEM

The approach we used to search for quenching of CO and CH_4 does not work well for N_2 and NH_3 . Indeed, Figure 10—the analog to Fig 4 for N_2 and NH_3 —shows no sign that quenching plays *any* role in the N_2 - NH_3 reaction, although doubtless quenching occurs.

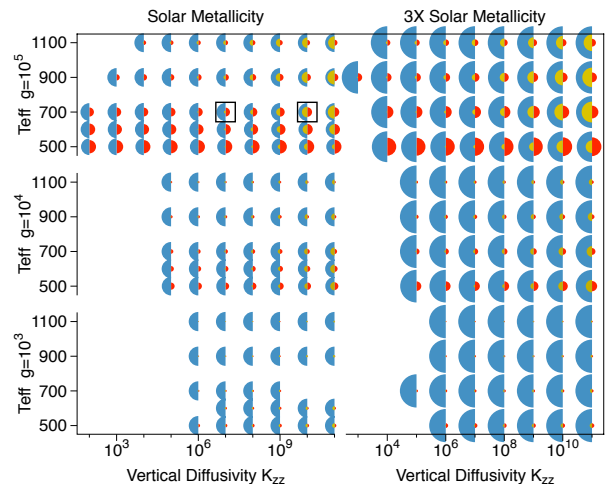


FIG. 10.— Nitrogen. The six panels are as in Fig. 4. Relative abundances of NH_3 (red, east) and N_2 (blue, west) are indicated by area. HCN abundances are multiplied by 5 to make them visible at lower g and superposed in gold on N_2 . Higher gravities and cooler temperatures favor NH_3 . The NH_3/N_2 ratio is insensitive to K_{zz} and only weakly sensitive to m , which suggests that NH_3 can be a proxy for g . HCN fares best at high g and high K_{zz} . The HCN/NH_3 ratio is sensitive to K_{zz} and only weakly sensitive to metallicity. The two boxed models are illustrated in Figure 11.

Two things get in the way. Of less importance, a third species—HCN—becomes non-negligible at high temperatures. HCN also quenches at high temperature, which

leaves the nitrogen system with three possibly distinct quench points: $\text{NH}_3\text{-N}_2$, $\text{NH}_3\text{-HCN}$, and $\text{N}_2\text{-HCN}$. Although HCN is never very abundant in equilibrium, it is often abundant enough that its decomposition can increase the NH_3 abundance by more than 10% after the $\text{NH}_3\text{-N}_2$ reaction has quenched. When confused with the second, greater obstacle, HCN can make it difficult to pinpoint where quenching occurs.

The greater obstacle is that curves of constant NH_3/N_2 are nearly parallel to the adiabat at the pressures and temperatures where quenching occurs. This is illustrated in Figure 11. Consequently the NH_3/N_2 ratio in a parcel remains close to equilibrium well after quenching has taken place, which makes the NH_3/N_2 ratio indifferent to quenching (Saumon et al. 2006). To show this, write the $\text{N}_2\text{-NH}_3$ equilibrium in the form

$$K_{\text{NH}_3\cdot\text{N}_2} = 5.90 \times 10^{-13} \exp(13207/T) = \frac{p\text{NH}_3^2}{p\text{N}_2 \cdot p\text{H}_2^3}. \quad (29)$$

Define $\xi \equiv \text{NH}_3/\text{N}_2$. If we approximate the total mixing ratio of N by $f_{\text{N}} \approx f_{\text{NH}_3} + 2f_{\text{N}_2}$ (including HCN makes this very complicated), we can write

$$\xi^2 \left(\frac{f_{\text{N}}}{2 + \xi} \right) = p^2 f_{\text{H}_2}^3 A e^{B/T}. \quad (30)$$

With context-obvious substitutions, the temperature gradient for contours of constant ξ is

$$\left(\frac{dT}{dp} \right)_{\xi} = \frac{2T}{B} \frac{T}{p} \approx 0.23 \frac{T}{1500} \frac{T}{p}. \quad (31)$$

The temperature gradient in Eq 31 is parallel to the adiabat (Eq 7) at 1750 K, and nearly parallel for $1500 < T < 2000$ K. For temperatures initially greater than 1750 K, the equilibrium ratio of NH_3/N_2 decreases as the parcel cools, reaching a minimum at ~ 1750 K where $(dT/dp)_{\xi} = (dT/dp)_{\mathcal{S}}$. If the parcel remains in chemical equilibrium, NH_3/N_2 will increase again as it cools further. This then is how we explain the insensitivity of NH_3/N_2 to K_{zz} seen in Figure 10: the NH_3/N_2 ratio computed by the full kinetics model is near the equilibrium value at the temperature where contours of NH_3/N_2 are parallel to the adiabat, which is also the minimum equilibrium value in the atmosphere. For the kinds of atmospheres considered in this paper, it appears that the amount of ammonia in the visible parts of the atmosphere will be comparable to the minimum equilibrium abundance computed along the adiabat.

On the other hand, because our results are insensitive to quenching, it is not difficult to find a non-unique chemical reaction time scale for the nitrogen system that predicts f_{NH_3} well. A chemical reaction time scale that works well in a quenching scheme that sets the reaction rate time t_{NH_3} equal to the mixing time $t_{\text{mix}} = H^2/K_{zz}$ is

$$t_{\text{NH}_3} = 1.0 \times 10^{-7} p^{-1} \exp(52000/T) \text{ sec}. \quad (32)$$

This particular choice presumes that the energy barrier is set by $\text{N}_2 + \text{H}_2 \rightarrow \text{NNH} + \text{H}$. This choice of t_{NH_3} is not unique. Almost any plausible choice of Arrhenius parameters that gives roughly the same time scale as Eq

32 at 10 bars and 1750 K will work just as well. We have no information to constrain dependence on p or m .

Figure 12 shows how our expression compares to some expressions in the literature. The chemical reaction time recommended by Lodders and Fegley (2002) is equivalent to

$$t_{\text{chem}} = \frac{1.2 \times 10^8 \exp(81515/T)}{p \cdot N \cdot f_{\text{H}_2}^2} \text{ sec}. \quad (33)$$

Equation 33 is based on the possible reaction $\text{N}_2 + \text{H}_2 \rightarrow \text{NH}_2 + \text{N}$. Figure 12 shows that Eq 33 used with $L = H$ gives as good a fit to our models as Eq 32. The extreme temperature dependence of Eq 33 appears justified.

Line et al. (2011) look for quenching in the reaction $\text{H}_2 + \text{N}_2\text{H}_2 \rightarrow 2\text{NH}_2$. Using rates given by Line et al. (2011), and using $p\text{N}_2\text{H}_2 = K_{\text{N}_2\text{H}_2} p\text{N}_2 p\text{H}_2$ with $K_{\text{N}_2\text{H}_2} = 3.8 \times 10^{-6} e^{-25738/T}$, we get

$$t_{\text{chem}} = \frac{1.3 \times 10^{11} T^{0.93} \exp(46400/T)}{N p f_{\text{H}_2}^2} \text{ sec} \quad (34)$$

as our best effort to reproduce their chemical time scale for NH_3 equilibration with N_2 . Figure 12 shows that Eq 34 agrees well with the predictions of our kinetics model when $m=3$, but sometimes predicts more NH_3 than we find for $m=1$. Disagreement is limited to cases with $K_{zz} < 10^7 \text{ cm}^2/\text{s}$, which means that Eq 34 is relatively fast at the lowest quench temperatures. It is possible that the temperature dependence of Eq 34 is not steep enough, or that the bottleneck involves N_2 rather than N_2H_2 , or that the highly uncertain thermodynamic parameters of NNH are being treated differently between models.

5.1. HCN-NH₃-N₂

The approach we used for CO and CH_4 works moderately well for HCN and NH_3 and less well for HCN and N_2 .

The equilibrium between HCN and CH_4 and NH_3 ,

$$K_{\text{HCN}\cdot\text{CH}_4} = \frac{p\text{CH}_4 \cdot p\text{NH}_3}{p\text{HCN} \cdot p\text{H}_2^3} = 3.0 \times 10^{-14} \exp(33460/T), \quad (35)$$

closely resembles the parallel equilibrium Eq 6 between CO and CH_4 . For the cool objects in which CH_4 is abundant at depth, the strong temperature dependence of $K_{\text{HCN}\cdot\text{CH}_4}$ means that HCN fares best with respect to NH_3 at high temperature when parcels move up or down along an adiabat.

For warmer worlds where CO and N_2 are dominant at depth, the most informative equilibrium is with CO, N_2 , H_2 , and H_2O , all of which are nearly constant when nearly all the C is in CO. The formal reaction is $2\text{CO} + \text{N}_2 + 3\text{H}_2 \leftrightarrow 2\text{HCN} + 2\text{H}_2\text{O}$, and the corresponding equilibrium constant is

$$K_{\text{HCN}\cdot\text{N}_2} = \frac{p\text{CO}^2 \cdot p\text{N}_2 \cdot p\text{H}_2^3}{p\text{HCN}^2 \cdot p\text{H}_2\text{O}^2} = 4.278 \times 10^{11} \exp(-528/T), \quad (36)$$

for which the temperature dependence is weak at quenching where $T_q \approx 2000$ K. Equation 36 indicates that $f_{\text{HCN}} \propto p$. Hence, in both the cool and the warm limits HCN increases with depth in deep atmospheres. Thus to identify HCN quenching it suffices to start from the

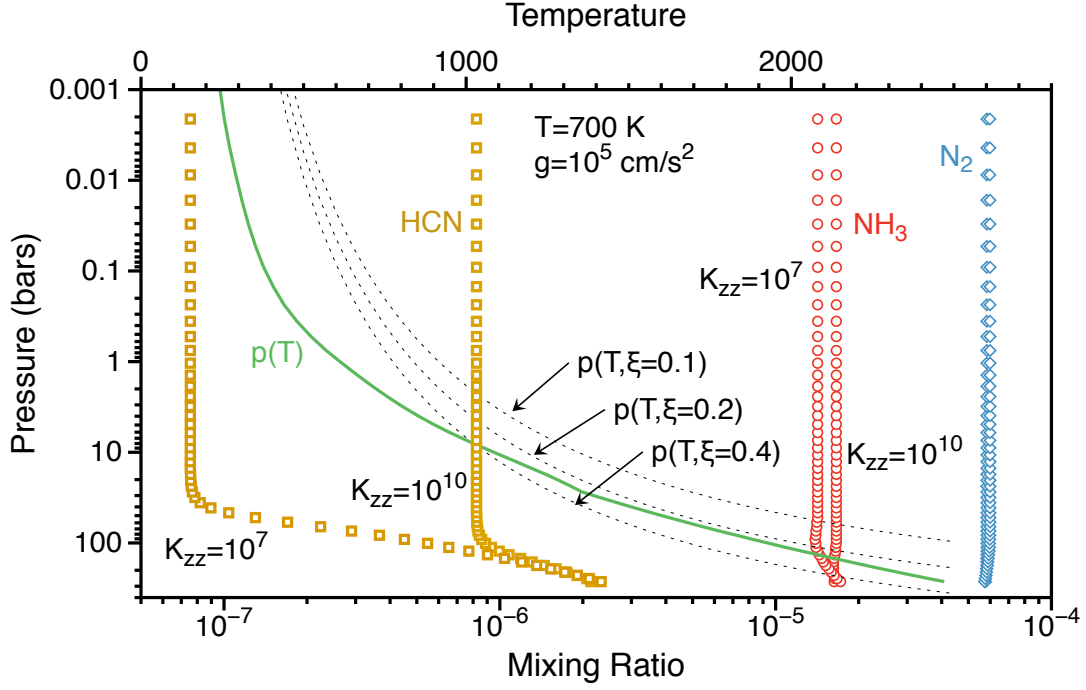


FIG. 11.— Two examples of quenching in nitrogen. The particular models are indicated by boxes on Figure 10. Volume mixing ratios of N_2 , NH_3 , and HCN are shown for two different K_{zz} pertinent to brown dwarfs. The relative insensitivity of NH_3 and N_2 to K_{zz} is a consequence of contours of constant NH_3/N_2 being nearly parallel to the adiabat $p(T)$. This is illustrated here by showing three relevant contours of constant $\xi \equiv \text{NH}_3/\text{N}_2$. Both ξ and $p(T)$ are plotted against the temperature axis (top). In the full models $\xi = 0.28$ and $\xi = 0.24$ for $K_{zz} = 10^{10} \text{ cm}^2/\text{s}$ and $K_{zz} = 10^7 \text{ cm}^2/\text{s}$, respectively.

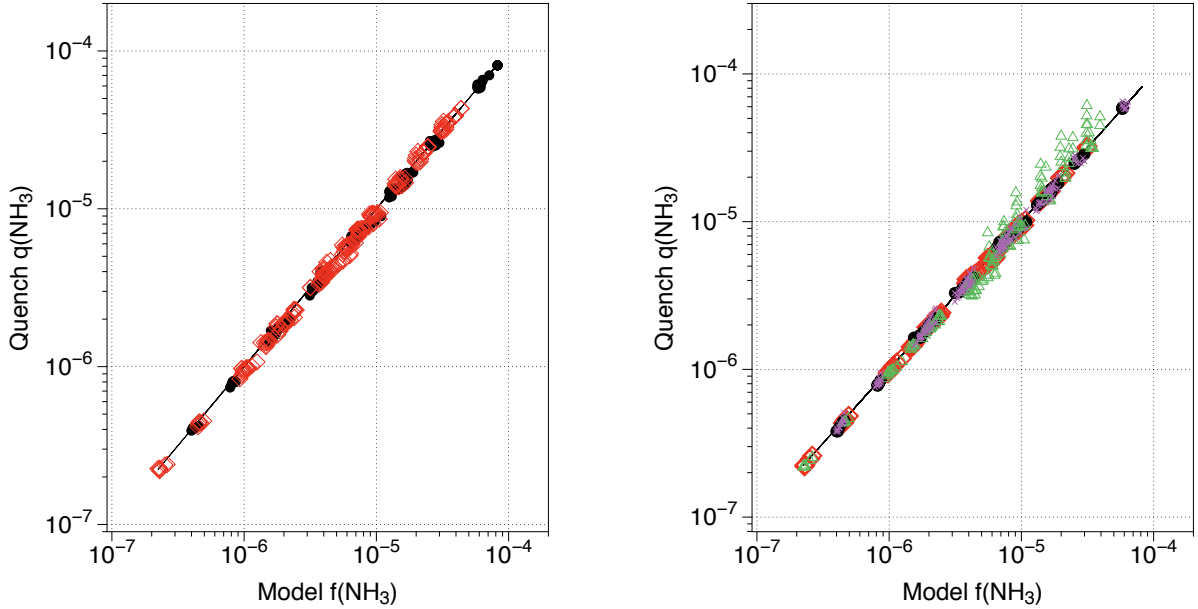


FIG. 12.— Ammonia predicted by the quenching approximation $q(\text{NH}_3)$ (y-axes) plotted against the actual asymptotic mixing ratio $f(\text{NH}_3)$ determined from the ensemble of 1-D kinetics models (x-axes). A perfect approximation would adhere to the line. Open red symbols are for $m=1$ and solid black symbols are for $m=3$. *Left.* Using Eq 32. *Right.* Open red diamonds $m=1$ and filled black circles $m=3$ are based on Lodders and Fegley (2002); open green triangles and purple crosses are based on Line et al. (2011).

bottom and find the altitude where the HCN abundance stops decreasing.

We looked for quench points defined against Eq 35, Eq

36, and a third equilibrium with CO and NH_3 ,

$$K_{\text{HCN}\cdot\text{CO}} = \frac{p_{\text{CO}} \cdot p_{\text{NH}_3}}{p_{\text{HCN}} \cdot p_{\text{H}_2\text{O}}} = 0.5025 \exp(6339/T). \quad (37)$$

Quenching with N_2 ($K_{\text{HCN-N}_2}$) gives an indifferent fit to an Arrhenius relation, as might be expected given the insensitivity of Eq 36 to f_{HCN} and the high thermal stability of N_2 . The other two equilibria both give plausible Arrhenius-like fits, although far from perfect (Figure 13).

A direct fit to the chemical time scale derived from the equilibrium $K_{\text{HCN-CH}_4}$ for the full ensemble of models is

$$t'_{q1} = 1.6 \times 10^{-4} p^{-1} m^{-0.7} \exp(37000/T) \text{ sec}, \quad (38)$$

whilst the corresponding fit to $K_{\text{HCN-CO}}$ is

$$t'_{q2} = 1.3 \times 10^{-4} p^{-1} m^{-1} \exp(34500/T) \text{ sec}. \quad (39)$$

At quench temperatures greater than 1600 K, the pressure dependence is better described by $t'_q \propto p^{-0.5}$, and the T dependence is stronger with an Arrhenius B -factor of order 46000 K. The stronger temperature dependence for high T_q suggests that reactions with N_2 with its high activation energy are becoming important. The higher T_q cases correspond to higher f_{HCN} .

As noted above, the quench approximation is not very sensitive to the details of t_q , and that is the case here as well. Computed quenched abundances using $t_q = t_{\text{mix}} = H^2/K_{zz}$ provide a good approximation to the HCN mixing ratios computed by the full model with

$$t_{\text{HCN}} = 1.5 \times 10^{-4} p^{-1} m^{-0.7} \exp(36000/T) \text{ sec}. \quad (40)$$

This expression seems to work well for all cases we have considered (Fig 14).

Fegley and Lodders (1996) treat HCN destruction as controlled by direct reaction of HCN with H_2 to make NH and CH_2 . The corresponding chemical time scale is

$$t_{\text{chem}} = \frac{9.3 \times 10^7 \exp(70456/T)}{N f_{H_2}^2} \text{ sec}. \quad (41)$$

This has a very steep temperature dependence. Quench approximations using Eq 41 with $L = H$ are shown in Figure 14. This approximation predicts much more HCN (a higher quench temperature) than we find in our 1-D models, a result consistent with the steep temperature dependence of Eq 41.

Moses et al. (2010) presume that HCN destruction is controlled by reaction of H_2 with the H_2CN radical. This is a much faster reaction. To convert their discussion into a reaction time requires defining the H_2CN equilibrium abundance. We write $pH_2CN = K_{H_2CN} \cdot pHCN \cdot pH$ with $K_{H_2CN} = 1.0 \times 10^{-6} e^{14240/T}$. This is likely not the same as what Moses et al. (2010) use. Atomic and molecular hydrogen are also assumed to be in equilibrium. Other pertinent information is given in Moses et al. (2010). The reaction time scale that results is

$$t_{\text{chem}} = \frac{8.3 \times 10^{20} \exp(23358/T)}{T^{1.941} N p^{0.5} f_{H_2}^{1.5}} \text{ sec}. \quad (42)$$

Figure 14 shows that Eq 42 used in a quench approximation predicts much less HCN than we compute in our 1D models. This means that reactions destroying HCN are occurring at relatively low temperatures. This fits with the relatively weak temperature dependence of t_{chem} in Eq 42.

The comparison of models may be frustrated in part by a hole in our model. We did not include methylamine

(CH_3NH_2), which Moses et al. (2010) argue plays the same role in hydrogenation of HCN at low temperatures and high pressures that methanol plays for CO. Their scheme is plausible but almost entirely hypothetical because it passes through several free radicals that must exist but about which little else is known. Our omission of a CH_3NH_2 channel implies that Eq 40 overestimates HCN, especially in cool worlds. Another issue undermining comparison between models is that we have not implemented Moses et al. (2010)'s full quench scheme: Moses et al. (2010) require that HCN quench with respect to already quenched abundances of CH_4 and NH_3 . But at the temperatures at which HCN might actually be abundant enough to be detectable in EGPs and BDs, our prescription should work and is easy to use.

6. CO_2

In principle CO_2 is also subject to quenching (Prinn and Fegley 1987), with caveats. First, because CO_2 quenches at a lower temperature than CO, it quenches with respect to the disequilibrium (quenched) abundance of CO. Second, in practice, CO_2 can be much enhanced by photochemistry if the world in question is subject to significant stellar irradiation. Under such conditions quenching is a poor guide. But for solitary brown dwarfs and planets in wide orbits it should do fine.

The approach is similar to that used for CO and CH_4 above. Equilibrium between CO_2 , CO, H_2 , and H_2O can be approximated by

$$K_{CO_2} = \frac{pCO \cdot pH_2O}{pCO_2 \cdot pH_2} = 18.3 \exp\left(-2376/T - (932/T)^2\right). \quad (43)$$

The equilibrium product Eq 43 is evaluated using the quenched values of pCO and pH_2O , beginning at the altitude where CO and CH_4 quench, and then extending to all higher altitudes. CO_2 quenching is pinned at the altitude where the equilibrium defined by Eq 43 breaks down. Figure 15 shows the results of doing so for the ensemble of models. Figure 15 is noisy because the deviations from equilibrium are modest and can go in either direction. It is interesting that the quenching timescale t_q varies inversely with the square root of the quench pressure p_q , and that unlike the CO- CH_4 system there is no discernible dependence on metallicity. The temperature dependence in the Arrhenius-like relation $t_q \cdot p_q^{0.5} \propto \exp(38000/T)$ is similar to the other cases we have looked at involving CO, which is also notable.

Figure 15 shows that CO_2 abundances in the ensemble of models are well approximated by a quench model provided that the appropriate disequilibrium CO and H_2O mixing ratios are used. A chemical reaction timescale that works well for CO_2 quenching is

$$t_{CO_2} = 1.0 \times 10^{-10} p^{-0.5} \exp(38000/T) \text{ sec} \quad (44)$$

where p is in bars. The results shown in Fig 15 are rather insensitive to the Arrhenius A factor in t_{CO_2} , which perhaps is to be expected given the weak temperature dependence of the equilibrium constant Eq 43 compared to the very strong temperature dependence of Eq 44.

7. DETECTABILITY

Whether or not a molecule can be detected depends on the abundance and opacity of the species in question

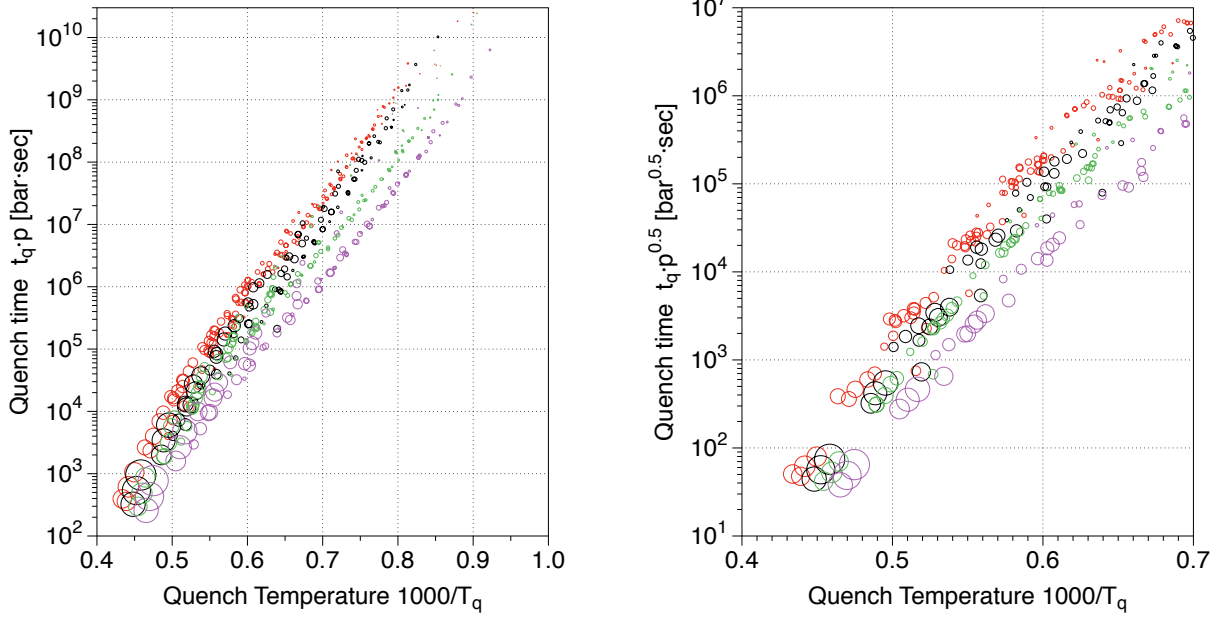


FIG. 13.— HCN quenching time scales determined from the ensemble of models with respect to NH_3 and CH_4 (red $m=1$ and black $m=3$) and CO (green $m=1$ and violet $m=3$). Symbol areas are proportional to f_{HCN} . *Left.* The time scale plotted is $t_q \propto p_q^{-1}$. *Right.* High T_q results fit better to the Arrhenius form with time scale $t_q \propto p_q^{-0.5}$.

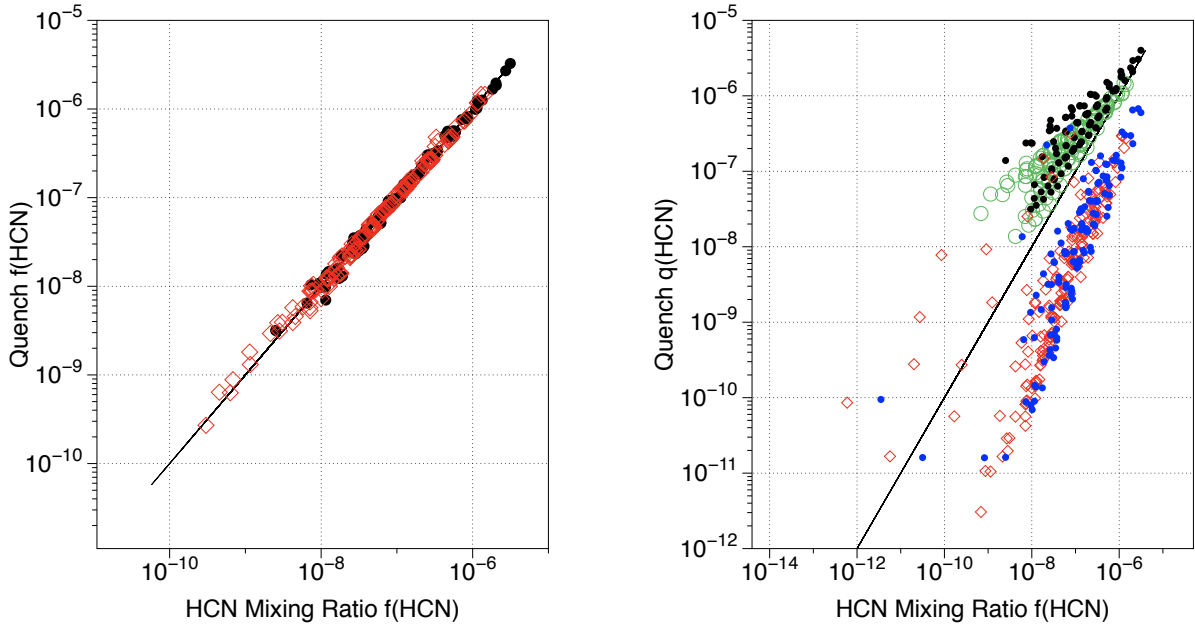


FIG. 14.— HCN mixing ratios predicted by various quenching approximations (y-axes) plotted against the actual asymptotic HCN mixing ratio as computed by the full ensemble of 1-D kinetics models (x-axes). A perfect approximation would adhere to the line. *Left.* Quench predictions using Eq 40. Open red symbols are for $m=1$ and solid black symbols are for $m=3$. *Right.* Quench approximations using Eq 41 with $L = H$ (open green circles, $m=1$; filled black circles, $m=3$) and using Eq 42 with $L = 0.14H$ (open red diamonds, $m=1$; filled blue circles, $m=3$).

and on the opacities of other molecules and clouds. For reference, Figure 16 shows absorption cross sections at 650 K and 1 bar pressure for H_2O , NH_3 , CH_4 , HCN , and CO . These can be compared to illustrative column densities shown in Figure 17. The latter are integrated upward from the 1, 0.1, and 0.01 bar pressure level, typical near-IR photospheric pressures for planets or brown dwarfs with gravities of 10^5 , 10^4 , and 10^3 cm s^{-2} , respectively. For CO , CH_4 , CO_2 , and HCN we plot column

densities for only one value of K_{zz} for each (g, T_{eff}) pair. We arbitrarily select $K_{zz} = 10^{13}/g$, a high value of K_{zz} but consistent with Eq 3, for the illustration. For N_2 and NH_3 we plot column densities for all K_{zz} to emphasize how little these depend on mixing.

While only a complete model spectrum can definitively predict the visibility of each molecule given a set of assumptions, we can use Figure 16 together with Figure 17 to make some generalizations. We defer the task of prop-

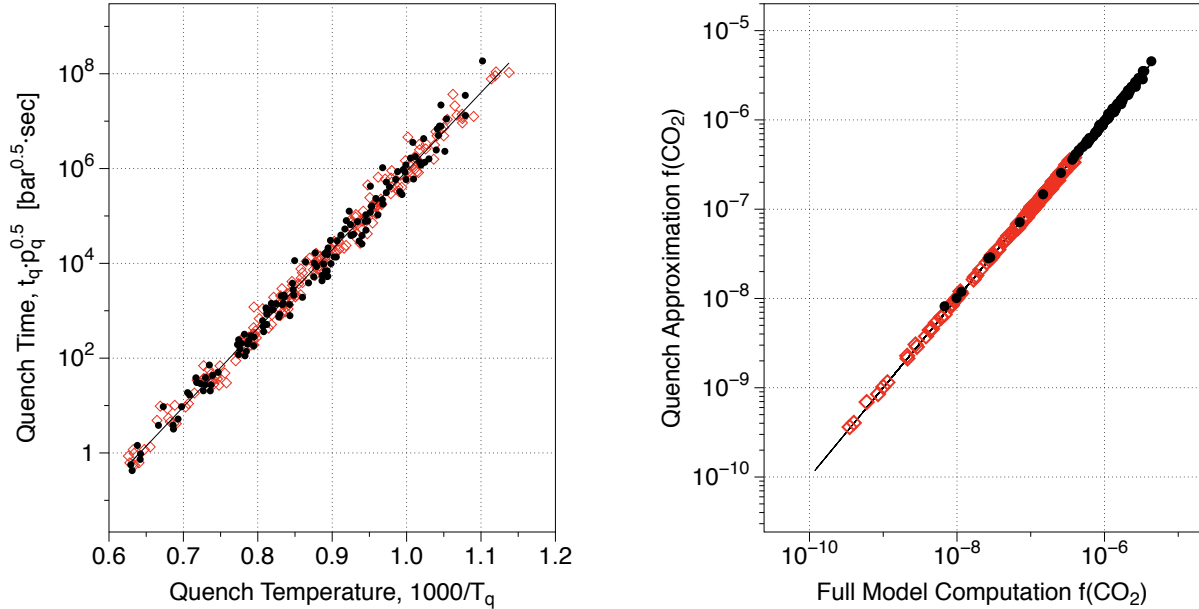


FIG. 15.— *Left.* CO_2 quenching time scales determined from the ensemble of models. Here quenching refers to disequilibrium between CO_2 and CO and H_2O ; CO and H_2O are themselves not in equilibrium because they have already quenched. The time scale plotted is $t_q \times p_q^{0.5}$. *Right.* f_{CO_2} predicted by the quenching approximation (y-axis) plotted against the actual asymptotic mixing ratio determined from the full ensemble of 1-D kinetics model (x-axis). A perfect approximation would adhere to the line. Open red symbols are for $m = 1$ and solid black symbols are for $m = 3$.

erly including our new chemical network into a complete model atmosphere to the future.

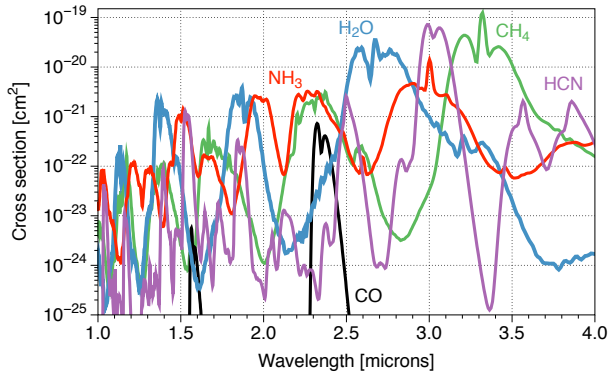


FIG. 16.— Absorption cross sections of molecules of interest here, computed at 650 K and 1 bar pressure, for wavelengths between 1 and 4 microns. UCL opacities are provided by the University College London and the Hitemp opacities are from the HITRAN opacity database (Rothman et al. 2003).

The absorption cross section per molecule for the CO band head at $2.3 \mu\text{m}$ is about 10^{-21}cm^2 per molecule. We know from model comparisons to data (e.g., Cushing et al. 2008) that by $T_{\text{eff}} = 1100 \text{K}$ at $g = 10^5$ this band head produces only a slight spectral feature. Consulting Figure 17 and scaling appropriately we expect, all else being equal, that CO would remain detectable down to $T_{\text{eff}} \sim 900 \text{K}$ at $g = 10^4$ and 500K at $g = 10^3$. This temperature is considerably cooler than expected by the conventional wisdom.

We likewise can consider the appearance of the $2.2 \mu\text{m}$ methane band which by definition first appears at the T0 spectral type at $T_{\text{eff}} \sim 1200 \text{K}$. Figure 17 suggests

that a comparable gravity-adjusted column abundance of methane will not appear in a Saturn-like $g = 10^3$ planet until $T_{\text{eff}} \sim 650 \text{K}$. The directly imaged companion GJ 504 b (Kuzuhara et al. 2013; Janson et al. 2013) provides a test of this reasoning. The mass and effective temperature of GJ 504 b have been estimated at $\sim 5 M_J$ and 600K . Its gravity should be $\sim 6000 \text{cm s}^{-2}$. By the reasoning above methane would be expected and indeed has been detected (Janson et al. 2013).

Methane is far more detectable in the $3.3 \mu\text{m}$ fundamental band where the absorption cross section is over an order of magnitude larger. CH_4 has been detected here as early as spectral type L5 (Noll et al. 2000) in field dwarfs. Likewise spectra over this wavelength range would better help to constrain the arrival of methane at low gravity in the directly imaged planets. Indeed Skemer et al. (2013) report a possible detection of this same feature in HR 8799 c, suggesting a trace abundance in the upper atmosphere.

Another test of these ideas may be provided by field T or Y dwarfs with unusual colors not predicted by models. Faint, red objects in particular would be good candidates for the low gravity, methane-poor objects we predict. For example the cool Y dwarf WISE 1828+2650 (Cushing et al. 2011), is both faint and unusually red in $J - H$ color (Beichman et al. 2014). While Cushing et al. did detect methane in this object, chemical equilibrium models do a very poor job fitting the available photometry (Beichman et al. 2014). Near-IR spectra should be obtained of all such color outliers to search for methane spectral features.

We note that some searches for planetary companions to young stars (e.g., Liu et al. 2010) as well as surveys for ‘planetary-mass’ T-dwarfs in young stellar clusters (e.g., Parker & Tinney 2013) have employed differential-methane band imaging. In this technique (Tinney et al.

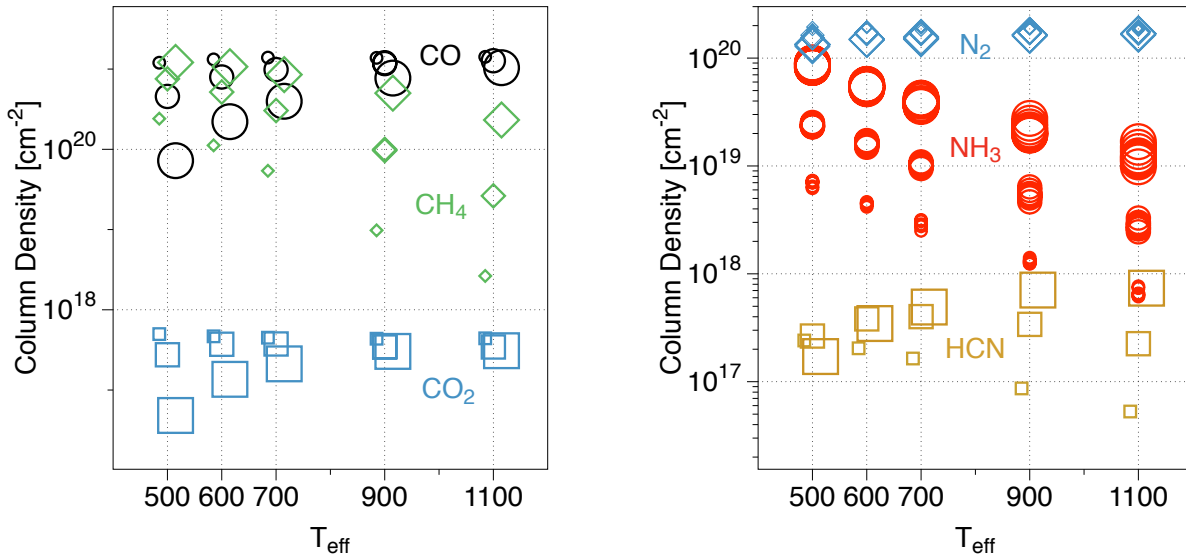


FIG. 17.— A sequence of models that illustrates how column densities of important carbon-bearing species change with temperature T_{eff} and gravity g . K_{zz} is restricted to $10^{13}/g$ for CO, CH₄, CO₂, HCN. All K_{zz} are plotted for N₂ and NH₃. Columns are integrated above $p = 10^{-5} \cdot g$ bars. Small symbols represent $g = 1000$, mid-sized symbols $g = 10^4$, and big symbols $g = 10^5$. *Left.* CO (black circles), CH₄ (green diamonds), CO₂ (blue squares). *Right.* N₂ (blue diamonds), NH₃ (red circles), HCN (gold squares).

2005) two images of a target are taken, one in a filter that matches the $1.7 - \mu\text{m}$ CH₄ band and one which probes the entire H band. When the two images are differenced, methane-bearing objects stand out as they are dark in the CH₄ filter. Our conclusions here suggest that such techniques must be used with caution as methane may simply not yet be present in planetary-mass objects even at effective temperatures below 1000 K.

Similar arguments can be made for the appearance of other spectral features of interest. We expect that NH₃ will appear at effective temperatures about 200 K cooler in planets compared to field brown dwarfs. HCN, with a cross section of 10^{-20} cm^2 per molecule at $1.55 \mu\text{m}$ is unlikely to be detectable in most objects as the computed column abundances are less than 10^{18} cm^{-2} . HCN's prospects are poor at 3.0 microns despite a high cross-section unless the C/O ratio is higher than solar and water's abundance reduced. Water's cross section is 100-fold smaller, but with solar abundances its column ($1 - 2 \times 10^{21} \text{ cm}^{-2}$) is 1000 times what HCN can reach at its best. Carbon dioxide has an absorption cross section 10^{-17} cm^2 per molecule at $4.2 \mu\text{m}$, and with abundances approaching 10^{18} cm^{-2} we expect it to be detectable at around 900 to 1100 K in field brown dwarfs. Indeed the AKARI space telescope discovered CO₂ features in several late L and early T dwarfs (Yamamura et al. 2010). Judging by Figure 17, we would predict CO₂ to be detectable to 500 K and cooler in the lowest mass planets.

8. CONCLUSIONS

We use a reasonably complete 1-D chemical kinetics code to survey the parameter space that encompasses atmospheres of cool brown dwarfs and warm young extra-solar giant planets. Our model contains only gas phase chemistry of small molecules containing H, C, N, O, and S. We use realistic p - T profiles for cloudless atmospheres with effective temperatures between 500 and 1100 K and surface gravities between 10^3 cm/s^2 to 10^5 cm/s^2 . Verti-

cal transport is described by an eddy diffusivity K_{zz} that we vary over a wide range. Our objective is to describe carbon and nitrogen speciation, especially at lower (planetary) surface gravities. Overviews of what we found are presented in Figure 4 for carbon and Figure 10 for nitrogen.

We find that carbon in cloudless brown dwarfs is predominantly in the form of methane at 900 K for $g = 10^5 \text{ cm/s}^2$. The small surface gravity of planets strongly discriminates against CH₄ when compared to an otherwise comparable brown dwarf. If vertical mixing is comparable to Jupiter's, methane first predominates over CO in planets cooler than 500 K. Sluggish vertical mixing can raise the transition to 600 K; clouds or more vigorous vertical mixing could lower it to 400 K.

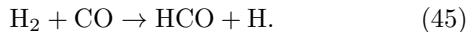
The detectability of specific molecular features in a spectrum depends on the strength of the molecular absorption cross sections as well as the gaseous abundance. Nevertheless a natural prediction of our model is that there will be cool planets with no methane observed in the H or K spectral bands. The refractory behavior of CO in low gravity objects is likely at least partially responsible for the lack of cool planets found by the NICI survey, which relied upon the methane absorption H band to identify planets (Liu et al. 2010).

Ammonia is also sensitive to gravity, but unlike methane and CO, ammonia is insensitive to mixing, which makes it a proxy for gravity. We did not explore temperatures low enough to determine the transition from N₂ to ammonia in planets, but it is nearly as abundant as N₂ at 500 K in brown dwarfs, which is broadly consistent with the observed properties of the Y dwarfs (Cushing et al. 2011) for which NH₃ is seen in H band. On the other hand, ammonia persists as an abundant minor species to rather high temperatures and this is consistent with it being readily detected in mid-IR spectra of T-dwarfs (Cushing et al. 2006). HCN might

become interesting in high gravity brown dwarfs if vertical mixing is very vigorous.

When expressed in terms of quenching parameters, nearly all our results for CO and CH₄ can be reduced to a simple equation in Arrhenius form that is easy to use but not easy to interpret. From a strictly practical perspective, what we find is close to what one gets using Prinn and Barshay (1977)’s algorithm in its original form (a fortuitous accident of using too high a rate for the wrong reaction). The apparent simplicity is somewhat surprising given the complexity of the chemistry involved and the many different ways the system has been described in the literature. Nor is our result quite what we expected. First, we find that the timescale t_{CO} for hydrogenation of CO is shorter for higher metallicity. Because the forward reactions that destroy CO have no metallicity dependence, we infer that metallicity dependence enters through the reverse reaction (oxidation of CH₄). By definition the reverse reaction is as fast as the forward reaction while in equilibrium, but it falls off more quickly than the forward reaction as the temperature drops. The important forward reactions are linear in metallicity whilst the important reverse reactions are quadratic in metallicity.

Second, we find that t_{CO} is inversely proportional to pressure. Analyses based on isolating a limiting reaction predict a stronger dependence on pressure, typically p^{-2} . The weaker p^{-1} pressure dependence is expected for a reaction involving CO itself, such as



It is interesting that R45 actually does have the highest ΔG value in the CO hydrogenation sequence, and therefore the highest energy barrier, and that the magnitude of ΔG of R45 is what we infer in Eq 14. But it is also quite clear from Figure 7 that equilibrium breaks down between CH₃OH and CH₄ well before it breaks down between CO and CH₃OH, as was found by Moses et al. (2011). Reactions involving CH₃OH imply a p^{-2} pressure dependence, because the equilibrium abundance of CH₃OH with respect to CO goes as the square of the H₂ pressure. The system behaves—both in the 40,000 K energy barrier and the p^{-1} pressure dependence—as if the overall rate depends on the entry reaction R45 rather than on the rate of R23 in which equilibrium actually breaks down. The apparent paradoxes might be resolved through a more complete analysis of the reverse reactions, or they may result from systematic biases stemming from our treating the mixing length as equal to a scale height, rather than as the complex function of many variables that it probably is (Smith 1998).

For nitrogen and ammonia we were unable to recover an emergent Arrhenius-like behavior from the full system. On the other hand, it was easy to devise a good quench approximation, and we also found that some published quench approximations (e.g., Fegley and Lodders 1994) work very well. For HCN, we met with mixed

success. We did find emergent Arrhenius-like behaviors, and we developed a new quench approximation that works quite well for our models. On the other hand there does not yet appear to be a consensus on what the quench chemistry of HCN actually is. We found a wide scatter of different outcomes when comparing different published quench schemes. We think our quench approximation should work well for warm objects where HCN is predicted to be relatively abundant but, because we did not consider hypothetical hydrogenation channels through methylamine (Moses et al. 2010), our models may overestimate f_{HCN} , especially in cooler objects.

There are many effects that our models do not address. None of these effects have much sway over our quench approximations, but they have much to do with what might actually be present in a real atmosphere.

Clouds are likely the most important. Adding infrared opacity to an atmosphere is effectively equivalent to reducing the gravity. This is because opacity raises the p - T profile (i.e., the adiabat) to a lower pressure for a given effective temperature. A cloudy atmosphere favors CO and N₂ over CH₄ and NH₃, other things equal. Increasing metallicity also increases opacity to the detriment of methane and ammonia.

Another issue for real worlds is that K_{zz} may be much smaller in higher altitude radiative regions of the atmosphere than it is in the convecting region. The radiative stratosphere is the part of the atmosphere where K_{zz} the modeling parameter is most suspect. For N₂ and NH₃ pronounced vertical structure in K_{zz} will not matter much. For CO and CH₄, sharply lower values of K_{zz} in the stratosphere might be important, because if K_{zz} is low enough, the atmosphere can have a second quench point in the stratosphere. Such behavior no problem to a full kinetics model, but it can make implementing quench approximations more complicated.

Photochemistry induced by irradiation from a nearby star can deplete NH₃ and increase CO₂ and HCN. Lightning and/or impact shocks in cool NH₃- and CH₄-rich atmospheres can generate CO and HCN (Chameides and Walker 1981). In warmer objects, catalysts that may be present in metallic clouds (here we mean real metals) will lower the quench point and thus will favor NH₃, CH₄, and CO₄ (Prinn and Fegley 1987).

All of these ideas will be put to the test by the directly imaged planets that are expected to be discovered in the coming months and years. Constraining the composition of their atmospheres will no doubt be a rewarding endeavour.

ACKNOWLEDGMENTS

The authors thank Richard Freedman, Caroline Morley, Julianne Moses, Didier Saumon, and Channon Visscher for many insightful discussions and occasional course corrections. The authors thank the NASA Planetary Atmospheres Program for support of this work.

REFERENCES

- Abelson, P. (1966). Chemical events on the primitive Earth. *Proc. Natl. Acad. Sci. USA* 55, 1365-1372.
- Barman, T., Macintosh, B., Konopacky, Q.M., Marois, C. (2011). Clouds and Chemistry in the Atmosphere of Extrasolar Planet HR8799b. *Astrophys. J.* 733, article id. 65, 18 pp.

- Barman, T., Macintosh, B., Konopacky, Q.M., Marois, C. (2011). The Young Planet-mass Object 2M1207b: A Cool, Cloudy, and Methane-poor Atmosphere. *Astrophys. J. Lett.* 735, article id. L39, 5 pp.
- Beichman, C., Gelino, C. R., Kirkpatrick, J. D., et al. 2014, *Astrophys. J.* 783, 68
- Bézar, B., Lellouch, E., Strobel, D., Maillard, J.-P., Drossart, P. (2002). Carbon Monoxide on Jupiter: Evidence for Both Internal and External Sources. *Icarus* 159, 95-111.
- Burcat, A., Ruscic, B. 2005, Third Millennium Ideal Gas and Condensed Phase Thermochemical Database for Combustion with Updates from Active Thermochemical Tables. Report ANL 05-20 and TAE 960.
- Burningham et al 2011, *MNRAS* 414, 3590.
- Burrows, A., Marley, M., Hubbard, W. B., et al. 1997, *ApJ*, 491, 856
- Chameides, W., Walker, J.C.G., Nagy, A.F. (1979). Possible chemical impact of planetary lightning in the atmospheres of Venus and Mars. *Nature* 280, 820-822.
- Chameides, W., Walker, J.C.G. (1981). Rates of fixation by lightning of carbon and nitrogen in possible primitive atmospheres. *Origins of Life* 11, 291-302.
- Cooper, C.S., Showman, A.P. (2006). Dynamics and Disequilibrium Carbon Chemistry in Hot Jupiter Atmospheres, with Application to HD 209458b. *Astrophys. J.* 649, 1048-1063.
- Cushing, M. C., Roellig, T. L., Marley, M. S., et al. 2006, *Astrophys. J.* 648, 614
- Cushing, M. C., Marley, M. S., Saumon, D., et al. 2008, *Astrophys. J.* 678, 1372
- Cushing, M. C., Kirkpatrick, J. D., Gelino, C. R., et al. 2011, *ApJ*, 743, 50
- Fegley, B.J., Lodders, K. (1994). Chemical models of the deep atmospheres of Jupiter and Saturn. *Icarus* 110, 117-154.
- Fegley, B.J., Lodders, K. (1996). Atmospheric Chemistry of the Brown Dwarf Gliese 229B: Thermochemical Equilibrium Predictions. *Astrophys. J. Lett.* 472, p.L37.
- Freytag et al (2010). *Astron. Astrophys.* 513, 19.
- Geballe, T. R., Saumon, D., Golimowski, D. A., et al. 2009, *Astrophys. J.* 695, 844
- Gierasch, P. J., & Conrath, B. J. 1985, Recent Advances in Planetary Meteorology, 121
- Haworth, N.L., Mackie, J.C., Bacskay, G.B. (2003). An Ab Initio Quantum Chemical and Kinetic Study of the NNH + O Reaction Potential Energy Surface: How Important Is This Route to NO in Combustion? *J. Phys. Chem. A* 107, 6792 - 6803.
- Hubeny, I., Burrows, A. (2007). A systematic study of departures from chemical equilibrium in the atmospheres of substellar mass objects. *Astrophys. J.* 669, 1248-1261.
- Janson, M., Brandt, T. D., Kuzuhara, M., et al. 2013, *Astrophys. J. Lett.*, 778, L4
- Jasper, A.W., Klippenstein, S.J., Harding, L.B. (2007). Secondary kinetics of methanol decomposition. *J. Phys. Chem. A* 111, 8699-8707.
- Kirkpatrick, J. D. 2005, *Ann. Rev. Astron. Astrophys.* 43, 195
- Kirkpatrick, J. D., Gelino, C. R., Cushing, M. C., et al. 2012, *ApJ*, 753, 156
- Konopacky, Q. M., Barman, T. S., Macintosh, B. A., & Marois, C. 2013, *Science*, 339, 1398
- Kuzuhara, M., Tamura, M., Kudo, T., et al. 2013, *Astrophys. J.* 774, 11
- Liang, M.C., Parkinson, C.D., Lee, A.Y.-T., Yung, Y.L., Seager, S. (2003). Source of atomic hydrogen in the atmosphere of HD 209458b. *Astrophys. J.* 596, L247-L250.
- Line, M.R., Liang, M.-C., Yung, Y.L. (2010). High-Temperature Photochemistry in the Atmosphere of HD 189733b. *Astrophys. J.* 717, 496-502.
- Line, M.R., Vasisth, G., Chen, P., Angerhausen, D., Yung, Y.L. (2011). Thermochemical and Photochemical Kinetics in Cooler Hydrogen-dominated Extrasolar Planets: A Methane-poor GJ436b? *Astrophys. J.* 738, article id. 32, 14 pp.
- Liu, M. C., Wahhaj, Z., Biller, B. A., et al. 2010, *Proc. SPIE*, 7736,
- Lodders, K. (2004). Revised and updated thermochemical properties of the gases mercapto HS, disulfur monoxide S₂O, thiazyl NS, and thioxophosphino PS. *J. Phys. Chem. Ref. Data* 33, 357-367.
- Lodders, K., Fegley, B.J. (2002). Atmospheric Chemistry in Giant Planets, Brown Dwarfs, and Low-Mass Dwarf Stars. I. Carbon, Nitrogen, and Oxygen. *Icarus* 155, 393-424.
- Marley, M.S., Fortney, J.J., Seager, S., Barman, T. (2007). An Imposing and Comprehensive Title. In *Protostars and Planets V*. Eds. B. Reipurth, D. Jewitt, and K. Keil. Univ. Ariz. Press, Tucson, pp. 733-747.
- Matus, M.H., Arduengo, A.J., Dixon, D.A. (2006). The heats of formation of diazene, hydrazine, N₂H₃⁺, N₂H₅⁺, N₂H, and N₂H₃ and the Methyl Derivatives CH₃NNH, CH₃NNCH₃, and CH₃HNNHCH₃. *J Phys Chem A.* 110, 10116-10121.
- Miller-Ricci Kempton, E., Zahnle, K., Fortney, J.J. (2011). The Atmospheric Chemistry of GJ 1214b: Photochemistry and Clouds. *Astrophys. J.* 745, 3 (13pp).
- Morley, C.V., Fortney, J.J., Kempton, E.M.R., Marley, M.S., Visscher, C., Zahnle, K.J. (2013). Quantitatively Assessing the Role of Clouds in the Transmission Spectrum of GJ 1214b. *Astrophys. J.* 775, article id. 33, 13 pp.
- Moses, J.I., Visscher, C., Keane, T.C., Spierdier, A. (2010). On the abundance of non-cometary HCN on Jupiter. *Faraday Discuss.*, 2010, 147, 103-136.
- Moses, J.I., Visscher, C., Fortney, J.J., Showman, A.P., Lewis, N.K., Griffith, C.A., Klippenstein, S.J., Shabram, M., Friedman, A.J., Marley, M.S., Freedman, R.S. (2011). Disequilibrium Carbon, Oxygen, and Nitrogen Chemistry in the Atmospheres of HD 189733b and HD 209458b. *Astrophys. J.* 737, article id. 15, 37 pp.
- Moses, J.I., Madhusudhan, N., Visscher, C., Freedman, R.S. (2013). Chemical Consequences of the C/O Ratio on Hot Jupiters: Examples from WASP-12b, CoRoT-2b, XO-1b, and HD 189733b. *Astrophys. J.* 763, article id. 25, 26 pp.
- Moses, J.I., Line, M.R., Visscher, C., Richardson, M.R., Nettelmann, N., Fortney, J.J., Barman, T.S., Stevenson, K.B., Madhusudhan, N. (2013). Compositional Diversity in the Atmospheres of Hot Neptunes, with Application to GJ 436b. *Astrophys. J.* 777, article id. 34, 23 pp.
- Moses, J.I. (2014). Chemical Kinetics on Extrasolar Planets. *Phil. Trans. Roy. Soc. A*. Fate Unknown.
- Noll, K. S., Geballe, T. R., & Marley, M. S. 1997, *Astrophys. J. Lett.* 489, L87
- Noll, K. S., Geballe, T. R., Leggett, S. K., & Marley, M. S. 2000, *Astrophys. J. Lett.* 541, L75
- Odd nitrogen production by meteoroids. *J. Geophys. Res.* 88, 4029-4035.
- Parker, S. R., & Tinney, C. G. 2013, *MNRAS*, 430, 1208
- Prinn, R.G., Barshay, S.S. (1977). Carbon monoxide on Jupiter and implications for atmospheric convection. *Science* 198, 1031-1034.
- Prinn, R.G., Fegley, B. (1981). Kinetic inhibition of CO and N₂ reduction in circumplanetary nebulae: Implications for satellite composition. *Astrophys. J.* 249, 308-317.
- Prinn, R.G., Fegley, B. (1987). Solar nebula Chemistry: origin of planetary, satellite, and planetary volatiles. In *Origin and Evolution of Planetary and Satellite Atmospheres*. Eds. Atreya SK, Pollack JB, Matthews MS, Univ of Arizona Press, pp 78-136.
- Rauk, A., Boyd, R.J., Boyd, S.L., Henry, D.J., Radom, L. (2003). Alkoxy radicals in the gaseous phase: beta-scission reactions and formation by radical addition to carbonyl compounds. *Can. J. Chem.* 81, 431-442.
- Rothman, L.S., et al. 2003, *J. Quant. Spect. & Rad. Tran.* 111, 2139.
- Saumon, D., Geballe, T. R., Leggett, S. K., et al. 2000, *Astrophys. J.* 541, 374
- Saumon, D., Marley, M. S., Cushing, M. C., et al. 2006, *Astrophys. J.* 647, 552
- Saumon, D., & Marley, M. S. 2008, *Astrophys. J.* 689, 1327
- Skemer, A. J., Marley, M. S., Hinz, P. M., et al. 2014, *Astrophys. J.*, in press, arXiv:1311.2085
- Smith, M.D. (1998). Estimation of a length scale to use with the quench level approximation for obtaining chemical abundances. *Icarus* 132, 176-184.
- Tinney, C. G., Burgasser, A. J., Kirkpatrick, J. D., & McElwain, M. W. 2005, *Astron. J.*, 130, 2326
- Visscher, C.W., Moses, J.I., Saslow, S.A. (2010). The deep water abundance on Jupiter: New constraints from thermochemical kinetics and diffusion modeling. *Icarus* 209, 602-615.

- Visscher, C.W., Moses, J.I. (2011). Quenching of carbon monoxide and methane in the atmospheres of cool brown dwarfs and hot Jupiters. *Astrophys. J.* 738, article id. 72, 12 pp.
- Visscher, C.W. (2012). Chemical timescales in the atmospheres of highly eccentric exoplanets. *Astrophys. J.* 757, article id. 5, 8 pp.
- Vuitton, V., Yelle, R.V., Lavvas, P., Klippenstein, S.J. (2012). Rapid association reactions at low pressure: impact on the formation of hydrocarbons on Titan. *Astrophys. J.* 744, article id. 11, 7 pp.
- Yamamura, I., Tsuji, T., & Tanabé, T. 2010, *Astrophys. J.* 722, 682
- Yung, Y.L., Drew, W.A., Pinto, J.P., Friedl, R.R. (1988). Estimation of the reaction rate for the formation of CH₃O from H + H₂CO: Implications for chemistry in the Solar System. *Icarus* 73, 516-526.
- Zahnle, K.J., Claire, M.W., Catling, D.C. (2006). The loss of mass-independent fractionation in sulfur due to a Paleoproterozoic collapse of atmospheric methane. *Geobiology* 4, 271-282.
- Zahnle, K.J., Haberle, R.M., Catling, D.C., Kasting, J.F. (2008). Mars Photochemistry Paper. *J. Geophys. Res.* 113, E11004, doi:10.1029/2008JE003160.
- Zahnle, K.J., Marley, M.S., Freedman, R.S., Lodders, K., Fortney, J.J. (2009). Atmospheric sulfur chemistry on hot Jupiters." *Astrophys. J. Lett.* 701, L20-L24.
- Zel'dovich, Ya.B., Raizer, Ya. (1967) *Physics of Shock Waves and High Temperature Phenomena, Vol. 2*, pp. 566-571, Academic Press, NY.